Tunable electronic and magnetic properties of two-dimensional materials and their one-dimensional derivatives

Zhuhua Zhang, Xiaofei Liu, Jin Yu, Yang Hang, Yao Li, Yufeng Guo, Ying Xu, Xu Sun, Jianxin Zhou and Wanlin Guo*

Low-dimensional materials exhibit many exceptional properties and functionalities which can be efficiently tuned by externally applied force or fields. Here we review the current status of research on tuning the electronic and magnetic properties of low-dimensional carbon, boron nitride, metal-dichalcogenides, phosphorene nanomaterials by applied engineering strain, external electric field and interaction with substrates, etc, with particular focus on the progress of computational methods and studies. We highlight the similarities and differences of the property modulation among one- and two-dimensional nanomaterials. Recent breakthroughs in experimental demonstration of the tunable functionalities in typical nanostructures are also presented. Finally, prospective and challenges for applying the tunable properties into functional devices are discussed. © 2016 The Authors. *WIREs Computational Molecular Science* published by John Wiley & Sons, Ltd.

INTRODUCTION

The past two decades have seen a bloom of research activities in nanoscience and a rapid development in delivering the potential of nanotechnology into diverse applications.[1] The major driving force for these activities and development is that nanoscale materials can offer novel electronic, magnetic, optical, mechanical, and chemical properties, which lead to distinguished performance in many technological fields, such as mechanic engineering, electronics, information, and energy technologies. The most intriguing behavior of nanomaterials is that their intrinsic properties are amenable to efficient modulation by applying various physical fields, in contrast to macroscopic systems.

In continuum, the functionality predominantly relies on the materials' bulk properties and thus only a small number of materials have useful responses to applied physical fields. As the materials and devices scale down to nanoscale, the timescale can be down to nanosecond (10^{-9} s), pico-second (10^{-12} s), and even femto-second (10^{-15} s). Accordingly, the energy scale changes from Joule (N·m) in macroscopic systems to 10^{-18} Joule (nN·nm, aJ) in nanosystems, which approaches the level of electron-volt (eV), namely the characteristic energy scale of local fields constituted by charge, molecular orbits, electron spins, and structures. Therefore, the physical fields (e.g., strain, electric and magnetic fields and substrates) applied to nanomaterials is prone to a strong coupling with the local fields and thereby remarkably changes the properties of systems, as shown in Figure 1(a). At nanoscale, the coupling between local and external fields can be remarkable even in materials that are featureless in their bulk counterparts,[2]

*Correspondence to: wlguo@nuaa.edu.cn

State Key Laboratory of Mechanics and Control for Mechanical Structures and Key Laboratory for Intelligent Nano Materials and Devices (MOE), Nanjing University of Aeronautics and Astronautics, Nanjing, China

Conflict of interest: The authors have declared no conflicts of interest for this article.
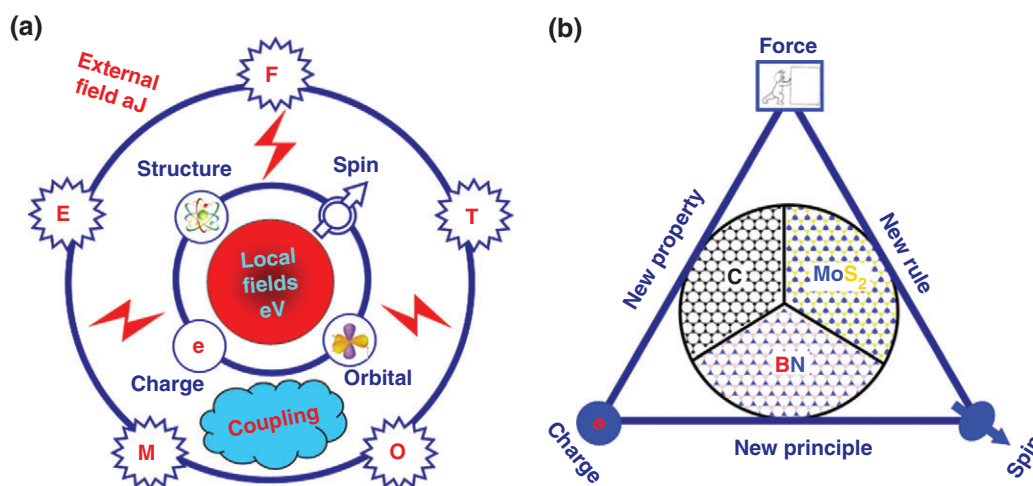
FIGURE 1 | (a) Coupling between local and external fields (F-force, E-electric field, M-magnetic field, O-optical, T-thermal) at nanoscale. (b) Tunable properties of typical low-dimensional materials, graphene, h-BN and MoS_2 by mechano-electro-magnetic coupling.

hatching out a series of tunable properties and functionalities and offering a wealth of opportunities for the development of nanoscience and the innovation in nanotechnology.

In terms of dimensionality, nanomaterials can exist in forms of zero-dimensional (0D) nanoclusters and nanoparticles, one-dimensional (1D) nanowires, nanotubes and nanoribbons, two-dimensional (2D) atomic crystals and nanofilms and 3D superstructures made of nanoscale components. In particular, the 1D and 2D nanomaterials, termed as low-dimensional materials, are the ideal systems for studying the peculiar nanoscale effects, which are of benefit not only for understanding fundamental phenomena under these dimensionalities but also for developing functional nanodevices with high performance. The 2D materials, represented by semimetallic graphene, insulating hexagonal boron nitride (h-BN) and semiconducting transition metal dichalcogenides MX_2 family (M = Mo, W; X = S, Se), have attracted most research attentions during the past decade. Graphene, a single-layer of graphite, possesses a number of extraordinary properties owing to its Dirac-like band dispersion at the Fermi level, but it has no bandgap to enable logic operation.[3] The h-BN monolayer, isostructural to graphene, is electrically insulating owing to the lack of inversion symmetry.[4] Differently, the semiconducting 2D MX_2 has metal-ligand bonding and a three-atom thickness, with the M atoms sandwiched between layers of X ligands. A notable technological advantage of these 2D materials is that they can be wrapped into cylindrical nanotubes and tailored into nanoribbons (Figure 2(a)). Quantum confinement effects enrich the nanotubes and nanoribbons with even more

fascinating functionalities and promise enhanced efficiency for electronic devices. Tuning the electronic and magnetic properties of these low-dimensional systems is always the object of extensive research, as tunable properties are highly desirable to allow great flexibility in design and optimization of functional devices. In this review, we focus on the mechano-electro-magnetic coupling effect and discuss the influence of strain, external electric fields and substrates on the electronic and magnetic properties of these materials (Figure 1(b)).

Since low-dimensional materials are structurally flexible and easy to deform, strain proves to be effective to tune their properties. In nanomaterials, strain not only changes atomic configurations, but also modifies the overlap of electron orbitals, charge distribution and bonding strength, providing a fertile ground for hatching novel properties. This behavior contrasts that of bulk materials where strain is related mostly simply to mechanical deformation. Nevertheless, the nanoscale strain effects differ from material to material and from 1D to 2D, and we are still in the dark about a universal mechanism for these effects in low-dimensional materials. Moreover, applied strain could also interplay with other physical quantities, such as electron spins in magnetic materials and electric polarization in polar materials, resulting in unusual piezomagnetic and piezoelectric effects. Achieving high efficiency and sensitivity for these effects is always pursued in related fields and calls for a development of current theoretical views.

Applying electric field is another common way toward achieving tunable properties. This is particularly suitable for low-dimensional materials since strong electric fields (e.g. from gates or interfaces) with strength in order of V/nm are prevalent in
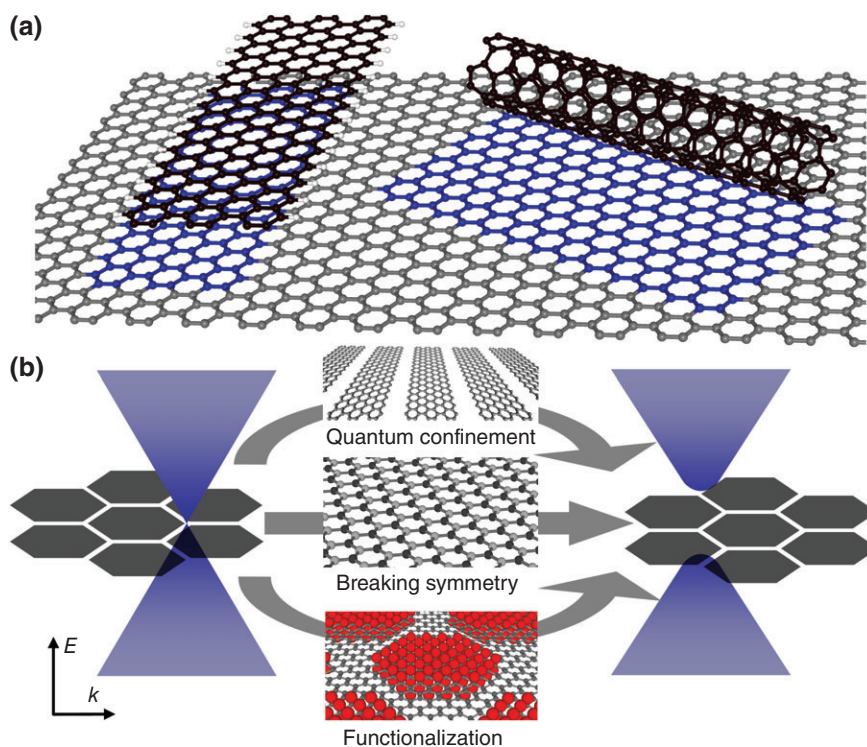
FIGURE 2 | Graphene nanostructures. (a) Atomic structures of graphene, which can be tailored into 1D nanoribbons and rolled into 1D nanotubes. (b) Schematic illustration of opening a bandgap in graphene, by tailoring into nanoribbons, breaking sublattice symmetry and chemical functionalization.

nanosystems. The electric field, either applied or built-in, can shift and split the energy levels of nanostructures, which, in turn, sensitively tunes the electronic structures. Also, external electric fields could drive charge transfer to electrically polarize the materials. In magnetic nanomaterials, the charge transfer alters the local spin population so as to modulate the magnetism of system. Moreover, the field-induced polarization can also couple to lattice structures, deforming the chemical bonds to induce electrostrictive effect. The progress on the electric field effects applies especially to theory-oriented works, while experimental research is still lingering behind. The major reason is that the involved electric field strength is too strong. Moreover, a great challenge remains in efficiently applying the fields to a target nanostructure. These issues stimulate further study of new principles and paradigms that are more feasible for achieving electric-field-tunable properties.

Strain and electric field effects in low-dimensional materials form the basis of mechano-electro-magnetic coupling at nanoscale. These effects enable precise control of material properties that is ideally suited for designing on-demand devices. While many exotic properties can stem from this nanoscale multiple-field coupling, they may be influenced by substrates or metal contacts that are unavoidable for device fabrication. Thus, fully understanding the impact of substrates on the material properties is also of central importance. The mechano-electro-magnetic coupling and substrate effects are essential for realizing functionality-oriented nanodevices. Toward this goal, experimentalists and theorists are required to make concerted efforts. Especially, for the sake of materializing many theoretically proposed concepts, it is important to improve the production and fabrication techniques that enable the realization of nanomaterials with atomic precision. In this contribution, we present a comprehensive state-of-the-art review on the tunable electronic and magnetic properties of low-dimensional materials and thoroughly summarize valuable achievements with respect to promising functionality modulation, novel device concepts, and prospective applications. We focus on 2D graphene and *h*-BN sheet and their 1D derivatives. Other newly emerged 2D materials, such as MX_2, phosphorene and MXenes will be accounted as well.

GRAPHENE NANOSTRCUTURES

Graphene

Single-Layer Graphene

Graphene exhibits many excellent properties, such as high electron mobility and long coherence length, due to a linear, Dirac-like energy dispersion near the Fermi level (Figure 2(b), left).[5] The charge carriers in graphene behave as massless Dirac fermions that can be sensitively modulated by electric, magnetic and strain fields. A major obstacle for graphene-based electronics is the inability to electrostatically confine electrons in graphene, which is semimetallic without a bandgap.[3] There are primarily three ways toward opening a bandgap in graphene (Figure 2(b)). The first way is to tailor graphene into graphene nanoribbons (GNRs).[6,7] A bandgap induced by quantum confinement effect can be opened in GNRs, whose edges can be further functionalized and shaped in various ways to achieve colorful properties,[8] as will be reviewed later; yet an efficient bandgap that suffices to allow logic operation at room temperature requires the ribbon width to be less than 10 nm[9] and the edges to be atomically smooth, which impose significant challenge on the fabrication. The second way is to form functionalized pattern in graphene by chemisorbing atomic species or forming antidot lattices.[10,11] The bandgap opened in this way can be up to 3 eV but the electronic mobility of graphene is sacrificed to a large extent by unintended localized electronic states. The third way is to break the symmetry between two sublattices by putting graphene onto a solid substrate[12] or applying electric fields to bilayer graphene.[13,14] Electrically gated bilayer graphene allows a good trade-off between the high carrier mobility and acceptable bandgap and also benefits from being compatible with traditional device architectures.

Gap opening in graphene is also amenable to applied magnetic fields, under which the Dirac fermions undergo an energy quantization,[3,15] manifested as a series of quantized Landau levels that can be expressed as

$$E_i = v_F \sqrt{2e\hbar B |i|}$$

where v_F is the Fermi velocity of graphene, B is the magnetic field strength and i is the index of the Landau levels. According to this expression, a vertical magnetic field of 45 T can open an energy gap of approximately 0.2 eV, which has been experimentally measured.[16] The magnetic-field-induced unusual quantum phenomena in graphene, such as the relativistic quantum Hall effect and electron correlation effects, have been thoroughly discussed in a recent review.[17] Of more interest is that the effect of vertical magnetic fields on the electronic properties of graphene can be mimicked by a distributed strain, which induces a pseudomagnetic field. Being designed to smoothly vary on the atomic scale, the strain deforms the Brillouin zone and shifts the Dirac cones away from the zone vertices (similar effect exists in carbon nanotubes (CNTs), as discussed later), resembling the effect of magnetic field induced on the charge carriers in graphene. Analytically, a 2D strain field leads to gauge-field vector potential A, which yields a pseudomagnetic field as $B = \partial A_y/\partial x - \partial A_x/\partial y$, where A is expressed as a tensor of strain gradient. Recent theories predicted a pseudomagnetic field of 10 T in graphene strained with triangular symmetry[18] and of 160 T in twisted GNRs hundreds of nanometers wide.[19] It has been experimentally reported that highly strained nanobubbles in graphene can induce a pseudomagnetic field greater than 300 T.[20] However, unlike a real magnetic field, the pseudomagnetic field does not break the time reversal symmetry in graphene since the strain-induced gauge-field vector potential always has opposite sign at the two graphene valleys (at K_1 and K_2 of the Brillouin zone).

In contrast to the effect of nonuniform strain, graphene can persist with its semi-metallic nature under a uniform isotropic strain up to 25%[21] or under a uniform shear strain up to 10%,[22] as these uniform strains cannot break the graphene inversion symmetry. Yet, uniaxial strain can bring evident anisotropy to the Fermi velocity of graphene, and, meanwhile, substantially increases the work function of graphene due to the raised vacuum level.

Bilayer Graphene

Bilayer graphene is special in that it can open a bandgap under applied vertical electric fields.[23] The electrically tunable bandgap only exists in Bernal (AB)-stacked bilayer graphene, rendering the controlled synthesis of high-quality bilayer graphene highly appealing.[24] In an electrically gated bilayer graphene, the measured carrier mobility reaches approximately 1000 cm^2 V^{-1} s^{-1} and the opened bandgap is up to 0.25 eV[25] (Figure 3(a) and (b)). The electronic properties of bilayer graphene are very sensitive to interlayer coupling. Guo et al. reported by *ab initio* calculations surprisingly high sensitivity of the field-induced bandgap of bilayer graphene to the change in interlayer spacing (Figure 3(c) and (d))[26]: a 10% compression of the spacing enhances
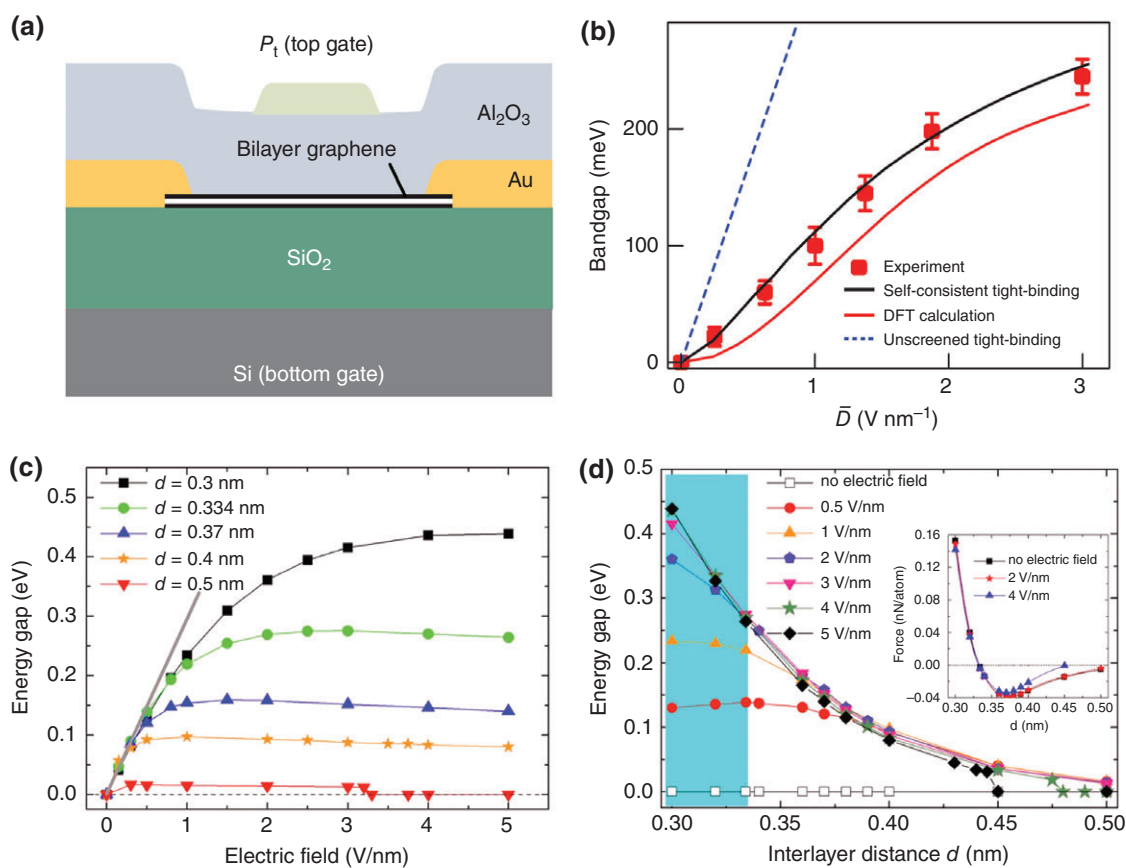
FIGURE 3 | Electrically tunable bandgap in bilayer graphene. (a) Schematic illustration of a side view of the electrically gated bilayer graphene. (b) Bandgap opened in graphene bilayer as a function of effective field strength. Theoretical results from self-consistent TB and *ab initio* methods are compared with experiments. (Reprinted with permission from Ref 25 Copyright 2009 Nature). (c) Bandgap as function of the field strength at different interlayer spacings *d*. The gray line on the left side of the curves indicates a universal linear scaling of the gap at low fields (below 0.3 V/nm) with a slope of 0.294 eV per V/nm for $d \leq 0.4$ nm. (d) Bandgap as a function of *d* at different electric fields. The shaded/clear regions on the left/right side correspond to compression/expansion of the spacing *d* from the equilibrium 0.334 nm. The inset in (d) shows the variation of interlayer force. (Reprinted with permission from Ref 26 Copyright 2008 American Institute of Physics).

the field-induced bandgap by 80% under a moderate field strength, suggesting that the electric-field-induced asymmetry in bilayer graphene can be enhanced by nanomechanical modulation. When epitaxially grown on a substrate, as in most device applications, bilayer graphene exhibits new behaviors due to interactions with substrate. The bottom layer chemically interacts with the substrate by hybridizing its π state with dangling bonds of the substrate,[13,27,28] whereas the top layer is usually *n*-doped due to charge transfer from the bottom layer and substrate. Structural defects or interlayer interaction with the bottom layer can open a small bandgap at the Dirac point of the top layer.[13] Further, applying bias voltage to bilayer graphene on C-terminated SiC substrate could induce a *n*-to-*p*-type transition, and vertical compression leads to an increase of the bandgap of the top layer.[29]

GNRs

GNR, a strip of graphene of nanometers in width (Figure 2(a)), exhibits richer properties and behaviors because of its edge states and width effects . GNRs with armchair edges (AGNRs) are semiconducting, mainly attributed to quantum confinement effect; GNRs with zigzag edges (ZGNRs) show magnetic edges states, which induce a staggered sublattice potential on the hexagonal lattice and result in a bandgap near the Fermi level.[7] The peculiar edge magnetism of ZGNRs has been experimentally confirmed, evidenced by a sharp change in the width-dependent bandgap in ZGNRs settled on a Cu substrate.[30] In reality, the edges of GNRs often show roughness, with many atomic steps protruded out of the edges.[31] Electronic and magnetic properties of the GNRs with periodic protruded edges are shown to depend on the length of the protruded step and step-
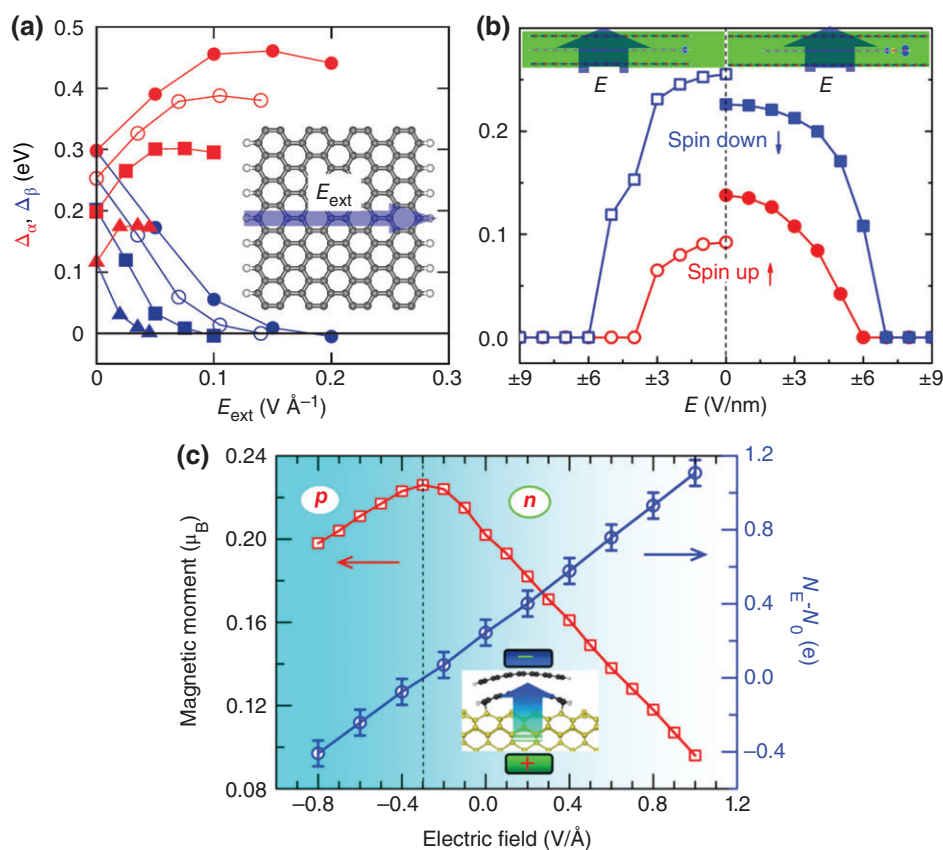
FIGURE 4 | Tunable electronic and magnetic properties of graphene nanoribbons. (a) Bandgaps of the spin-up (red) and spin-down (blue) channels of zigzag graphene nanoribbons as functions of field strength. Model illustration of applying transverse electric field to a zigzag nanoribbon. (Reprinted with permission from Ref 34 Copyright 2006 Nature). (b) Half-metallicity in zigzag graphene nanoribbons sandwiched between zigzag BN nanoribbons under bias voltage. Bandgaps of the two spin channels as functions of field strength for two systems with different ribbon widths (see insets) (Reprinted with permission from Ref 35 Copyright 2013 American Chemical Society). (c) Magnetoelectric effect in a bilayer graphene nanoribbons on Si(001). Magnetic moment per edge carbon atom in the top layer (red line) and amount of charge transferred to the top layer (blue line) as functions of field strength. Inset: atomic illustration of a bilayer nanoribbon adsorbed on Si(001). (Reprinted with permission from Ref 36 Copyright 2009 American Physical Society).

to-step distance along the ribbon edge.[32] With a small step length, the GNR evolves from a nonmagnetic semiconductor, via metal, to a magnetic semiconductor with increasing inter-step distance. Electronic transport study of GNRs with edge irregularity showed that the edge roughness increases the minimal leakage current due to the localized states induced in the bandgap and decreases the on current due to smaller quantum transmission,[33] from which, however, a transistor switching behavior is survived.

Tunable Magnetism in GNRs
Tuning the electronic and magnetic properties of GNRs is of special interest from both fundamental and technological perspectives. The ZGNRs have been intensively studied in this aspect. Applying transverse electric field (Figure 4(a)) or decorating the edges with different chemical groups is predicted to

make half-metal from ZGNRs.[34,37,38] Still, there is no experimental support to the half-metallic ZGNRs. The major issues contain: (1) the magnetic state in ZGNRs is very sensitive to edge quality and termination; (2) the magnetism is relatively weak and easy to be quenched by thermal activation; (3) it is challenging to effectively apply a strong electric field required for the half-metal to a target ZGNR. Very recently, Yu et al. proposed a new paradigm (Figure 4(b)) that can realize the half-metal in ZGNRs by applying bias voltages. They sandwiched a ZGNR between two h-BN nanoribbons (BNNRs); then applied bias voltage or vertical compression can tune the system into half-metal,[35] due to increased electric polarization by the h-BN layers which enhances the exchange potential across the GNRs.

The semiconductor to half-metal transition can also be induced in bilayer GNRs. Guo et al. found that a bilayer ZGNR with antiferromagnetic coupling

between the opposite edges can be tuned into half-metal by applying transverse electric field or strain.[39] The bandgap of a bilayer ZGNR decreases with decreasing interlayer spacing until it is closed. To promote applications, Zhang et al. placed the bilayer ZGNR on silicon substrate and found tunable magnetoelectric effect (Figure 4(c)).[36] They showed that an applied bias voltage drives charge transfer between the nanoribbons and substrate, which controls the exchange splitting of magnetic edge states and hence the edge magnetic moment. In particular, the bias induced *n*-to-*p*-type transition in the top ribbon layer can switch the magnetoelectric coefficient from negative to positive. For a monolayer ZGNR adsorbed on Si(001) substrate, the edge magnetism completely disappears due to the formed Si–C bonds at ribbon edges[40]; yet the ZGNR can be semiconducting or metallic depending on the ribbon width and adsorption orientation. These findings pave the way for fabricating graphene-based electronic and spintronic devices by integrating with existing silicon technology.

Strain Effect in GNRs

The electronic structure of GNRs is tunable by strain. Theoretical studies showed that the electronic properties of ZGNRs are insensitive to uniaxial strain, while the bandgap of AGNRs changes in a zigzag pattern with uniaxial strain.[41,42] This stands in stark contrast to graphene, whose semimetallic nature can persist at a uniaxial strain up to 25%.[21] In addition, twisting AGNRs can also couple the conduction and valence bands and linearly modulate the bandgap, with the slope of gap versus twist angle depending on the ribbon width.[43] Moreover, in suspended GNRs, twisting couples with axial tensional strain and therefore leads to larger modulation of bandgap that manifests as a non-linear function of twist angle.[44] The underlying physics for the strain-tunable bandgap in AGNRs is similar to that in CNTs, since the bandgaps in both CNTs and AGNRs essentially share the same origin that is due to the quantized momentum along the transverse or circumferential direction (see related discussion on CNTs later). The electromechanical responses in the AGNRs could be exploited in switches and sensor applications.

CARBON NANOTUBES

Basic Properties

Single-Walled CNTs

CNTs were first characterized by Iijima in 1991 using electron microscopy.[45] A single-walled CNT (SWCNT) is geometrically made up by rolling a graphene sheet into a cylinder along a specific direction. The structure of a SWCNT can be characterized by a chiral vector, $C_h = na_1 + ma_2$, or a chirality index (n,m), where a_1 and a_2 are two basic vectors of graphene lattice. SWCNTs with a specific chirality have been realized by controlled synthesis methods.[46,47] The chiral angle θ can be obtained by $\sin\theta = \sqrt{3} m/(2\sqrt{(n^2 + nm + m^2)})$. Armchair and zigzag CNTs correspond to $\theta = 30°$ and $0°$, respectively, as shown in Figure 5(a). The CNT diameter can be geometrically expressed as $D = a\sqrt{(n^2 + nm + m^2)}/\pi$, where a is the lattice constant of graphene. In early CNT synthesis, the CNT diameter can vary from hundreds of nanometers to sub-nanometer. In 2000, small CNTs with diameters of 0.5[49] and 0.4 nm[50] were reported. Meanwhile, Peng et al. observed a small SWCNT with diameter of 0.33 nm, which exists as a tiny branch on a parent CNT.[51] Three years later, Zhao et al. observed a 0.3-nm-diameter (2, 2) CNT as the innermost wall of a multi-walled CNT (MWCNT),[52] which should be the smallest CNT reported thus far. Along the longitudinal dimension, the longest CNTs can reach 2 mm in 1998[53] and recently this record was updated to 550 mm,[54] rendering the CNTs a bridge connecting the nanoscale matters to the macroscopic world.

Multi-Walled Carbon Nanotubes

A MWCNT is comprised of two or more concentrically aligned SWCNTs, being either periodic or aperiodic depending on the interwall commensurability. An important topic on MWCNTs is the chirality correlation of different tube walls. A number of experiments using different synthesis methods yield MWCNTs with identical or nearly identical chiralities when the growth temperatures are relatively low.[55–57] Using molecular dynamics simulations with chirality-related potential, Guo et al. found[58] that, for a MWCNT with a diameter more than 12 nm, nearly identical chiralities correspond to the energy optimum; for a MWCNT with diameter less than 10 nm, the chiral angle ratio of the outer to inner walls decreases with decreasing tube diameter, and the nearly identical zigzag chiralities are preferred when the tube diameter becomes very small.

Electronic Structures of Carbon Nanotubes

Understanding electronic structures of CNTs needs to start from graphene, which has a zero bandgap with the valence and conduction bands met at two vertexes of the Brillouin Zone, K_1 and K_2 (Figure 5 (b)). The dispersion around the vertex is a cone.

(a)

(b)

(c)
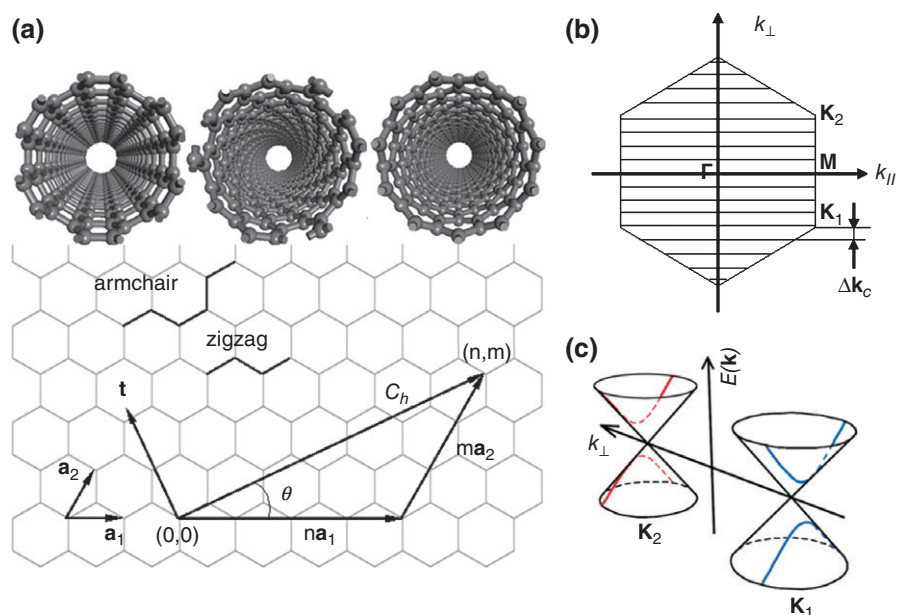
FIGURE 5 | Structure and electronic properties of CNTs. (a) Schematic diagram showing how a graphene sheet is wrapped to form a CNT along a chiral vector $n\mathbf{a}_1 + m\mathbf{a}_2$, where $\mathbf{a}_1$ and $\mathbf{a}_2$ are the basic vectors of graphene. The insets show atomic structures of an armchair, a chiral and a zigzag CNT. (b) Hexagonal Brillouin zone of graphene and the quantized wave vector $\mathbf{k}_c$ (horizontal lines) along the CNT circumference. The allowed $\mathbf{k}_c$ miss the vertexes K_1 and K_2 of the Brillouin zone by an amount $\Delta\mathbf{k}_C$. (c) Slicing the dispersion cones by allowed $\mathbf{k}_c$ gives the electronic structure of a CNT near the Fermi level. (Reprinted with permission from Ref 48 Copyright 2004 Nature).

Upon wrapping into a CNT, the electronic wave vector in the circumferential direction, $\mathbf{k}_c$, is quantized and satisfies a boundary condition $\pi D \mathbf{k}_c = 2\pi j$, where j is an integer; the as-allowed values of $\mathbf{k}$ are represented by the horizontal lines in Figure 5(b) that miss K_1 or K_2 by an amount $\Delta\mathbf{k}_c$. The CNT electronic structure near the Fermi level is determined by the Conic section of the dispersion cones by allowed $\mathbf{k}_c$ (Figure 5(c)). When n-m is a multiple of 3, $\Delta\mathbf{k}_c = 0$, thus the corresponding CNT is metallic; otherwise it is a semiconductor. The energy distance between the upper and lower branches of the Conic section defines the CNT's bandgap.[48] The semiconducting CNT has its bandgap decreasing with increasing tube diameter D and in the limit of $D \to \infty$ it converges to the semi-metallic graphene. When $D < 0.5$ nm, all CNTs become metallic independent of chirality due to curvature-induced rehybridization of σ and π orbitals.[59]

In mechanical aspect, a pristine SWCNT possesses an extremely high elastic modulus over 1 TPa,[60,61] comparable to that of diamond. A SWCNT can also withstand >12% tensile strain, two orders higher than that of steel. The tensile strength of CNTs can range from 20 to 63 GPa[62] depending on diameter while the compressive strength can reach up to 100 GPa.[63] In the radial direction, CNTs are rather flexible and the compressive strength is estimated to be over 5.3 GPa.[64] However, CNTs usually contain defects, such as dislocation (5|7) defects, vacancies, or impurities, which can dramatically influence the electronic and mechanical properties of CNTs. For example, a 5|7 defect can produce two quasi-bound states and reduce the conductance by one quantum unit at the corresponding energy.[65] The tensile strength can degrade to 60% of the ideal value in the presence of vacancies.[66]

Mechano-Electro-Magnetic Coupling Effect in Carbon Nanotubes

Electromechanical Coupling
SWCNTs can be subject to various deformations, which are able to induce remarkable electromechanical coupling. As discussed, the electronic structure of a SWCNT is determined by chirality-dependent position of quantized wave vectors $\mathbf{k}$ (along the tube circumference) relative to the Fermi point $\mathbf{k}_F$ at K_1 and K_2. Applied uniaxial and torsional strains shift the Fermi point away from the K_1 and K_2, change $|\mathbf{k}$-$\mathbf{k}_F|$ or $\Delta\mathbf{k}_c$ and thus modify the bandgap of CNTs
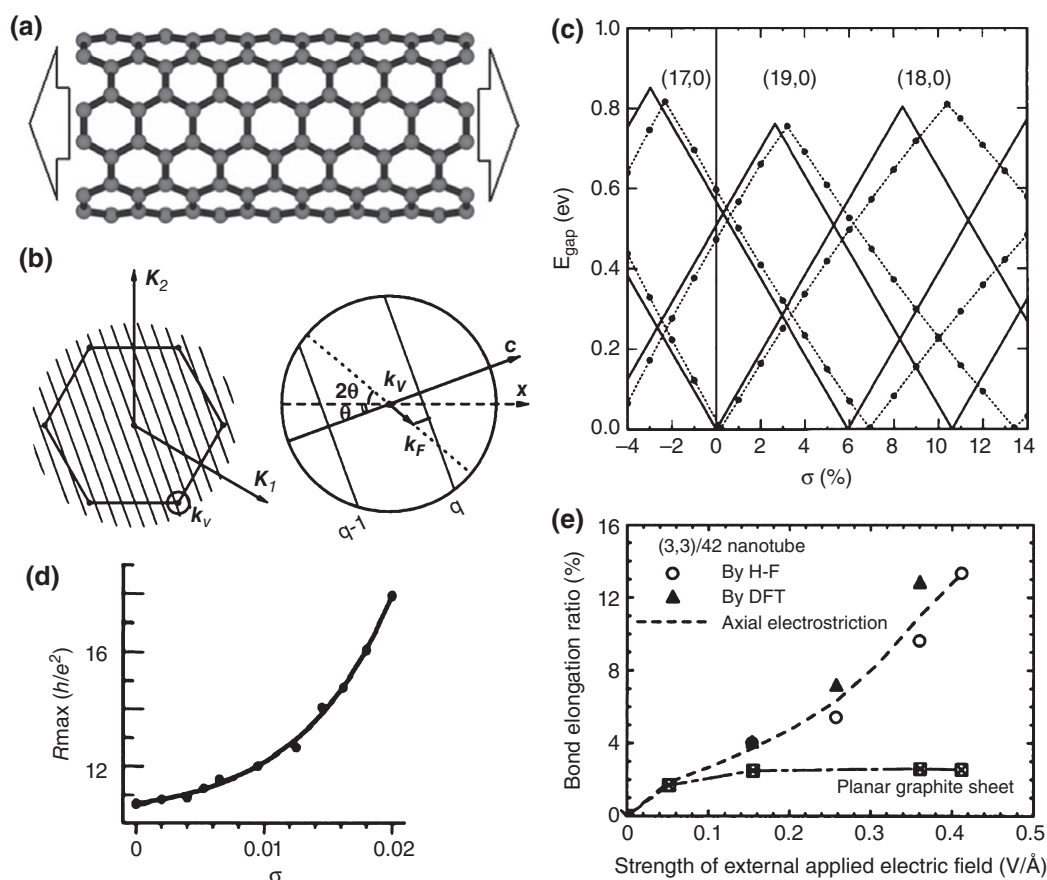
FIGURE 6 | Electromechanical coupling in CNTs. (a) Illustration of a zigzag CNT under uniaxial strain. (b) Hexagonal central Brillouin zone and k parallel lines for allowed electronic states. k_F is driven away from the vertex K_1 by uniaxial strain with an angle of 3θ from axis c, for $n-m = 3q-1$, where q is a positive integer. (c) Bandgaps of three SWNTs as functions of uniaxial strain, obtained from theory (solid lines) and simulations (dashed lines and symbols). (Reprinted with permission from Ref 67 Copyright 2000 American Physical Society). (d) The maximum resistance of a CNT device as a function of uniaxial strain (Reprinted with permission from Ref 68 Copyright 2003 American Physical Society). (e) Average bond elongation ratios in the (3, 3) CNT with 42 carbon atoms and the corresponding unfolded graphene sheet as functions of external electric field strength. (Reprinted with permission from Ref 69 Copyright 2003 American Physical Society).

(Figure 6(a) and (b)). The electronic structure of deformed CNTs depends on the chirality and deformation mode, which can be well described by the Hückel tight-binding (TB) model[67]

$$H_j(\mathbf{k}, \xi) = H_j^0(\mathbf{k})\tau_j \left(\exp i\mathbf{k} \bullet \Delta\mathbf{r}_j \right) \qquad (1)$$

where ξ represents a 2D strain tensor, $\Delta\mathbf{r}_j$ is the deformation of jth ($j = 1,2,3$) bond vector, and H^0 is the Hamiltonian matrix element for an undeformed SWCNT. From this model, the change of CNT bandgap versus strain exhibits a zigzag pattern, with a periodicity reversely proportional to the tube diameter (Figure 6(c)). Specifically, the bandgap of zigzag CNTs is most sensitive to uniaxial strain yet most impervious to torsional strain; the opposite holds for

the armchair CNTs. The strain-tunable bandgap of CNTs was confirmed in subsequent experiments, which showed that a uniaxial strain can open a bandgap in a metallic CNT and increase the electric resistance of CNTs (Figure 6(d)).[68] The strong electromechanical coupling in CNTs has opened potential applications for nanoelectromechanical devices.[70]

Compared to high axial stiffness, a SWCNT is much more flexible in the radial direction and pone to radial deformations. Early in 1999, Park et al. reported with *ab initio* calculations that the CNT bandgap can be easily opened or closed by radial deformations.[71] Later on, using a TB molecular dynamics, Lu et al. found a metal-to-semiconductor transition in squashed armchair CNTs,[72] attributed to a combined effect of broken mirror symmetry and bond formation between flattened regions of tube wall. In 2005, a more

conclusive analysis on the squashed armchair CNTs was performed by Mehrez et al.,[73] showing that the squashed armchair CNTs can restore to metallic at sufficiently high deformation even if the CNTs undergo a breaking of mirror symmetry, thanks to strong π-σ hybridization. A metal–insulator CNT junction can be designed via local collapse of the nanotubes by, for example, depositing insulating layers. In addition, CNTs are easy to bend, in either local or uniform manner. The local bending leads to the mixing of σ and π states yet without gap opening in metallic CNTs. The electronic transport through a locally bent CNT is essentially unaffected unless the bending is large enough to introduce backscattering to decrease the conductivity.[74,75] In contrast, a uniform bending keeps the states delocalized over the entire CNTs[76] and modifies the bandgap, depending on the chirality as analyzed by Chibotaru et al.[77] Transport study also supported that uniform bending decreases the conductivity through a metallic CNT but increases that through a semiconducting CNT[78]; as the bending becomes severer, kink structures appear at the inner side of the CNT and break the monotonic dependence of the conductivity on deformation.

The electromechanical coupling can also manifest as the interaction between electric fields and CNT lattices. First, electric fields strongly affect the structure and strength of CNTs. Several theoretical studies[79,80] showed that the CNT failure under electric fields[79] or charge[80] preferentially occurs at tube ends, to which adding caps can enhance the nanotube stability. Under a tensile load, Guo et al. found that the CNT breaks near its middle and its critical tensile strength declines significantly with increasing field strength.[81] Subsequent experiments confirmed these theoretical results and further showed that the tube failure could also occur at defects on the tube wall.[82] On the other hand, the mechanical and electric behaviors are always coupled with each other in CNTs. The design of CNT nanomemory is just based on the coupling of mechanical bending and electrostatic attraction.[83] Under applied electric fields, the charge density in a CNT will be redistributed because of electric polarization near the ends so that the tube is locally not electrically neutral. This in turn causes the CNT to be stretched by electric fields. Guo et al. found that a SWCNT can be axially stretched up to 10% under a field strength less than 1 V/Å[69] (Figure 6(e)). The giant electrostrictive deformation, together with the high stiffness of CNTs, opens a promising prospect for developing high-efficiency energy conversion devices. Another behavior worth mentioning is that CNTs can stretch (by ~1%) upon charge injection, contributed by a uniform deformation of C–C bonds due to the change in the population of electron orbitals.[84] CNT actuators and sensors have been designed based on this effect.[85]

Electromagnetic Coupling in Carbon Nanotubes

In CNTs, the electron and hole sub-bands have 1D feature, and their electronic states resemble semiclassical electron orbits encircling the nanotube. An electron moving along these orbits has an orbital magnetic moment μ_{orb},[86] expressed as $\mu_{orb} = Dev_F/4$, where v_F is the Fermi velocity of electrons. According to Zeeman effect, an applied axial magnetic field can shift the energy of sub-bands by $\Delta E = -\mu_{orb} \cdot \mathbf{B} = \pm Dev_F B_{\parallel}/4$.[48] This equation provides a simple relationship between the CNT bandgap and the magnetic field strength and accounts for experimental observations of giant magnetoresistance and metal–insulator transition in CNTs under axial magnetic fields.[87] However, this equation cannot give the detailed electronic structures of CNTs under a magnetic field, which are necessary for understanding other important magnetic properties, such as magnetic susceptibility. For this purpose, the effective-mass approximation and TB model have been employed. Since the effective-mass approximation is valid only at the charge-neutral state and only provides the information about the electronic states near the Fermi level,[88] we focus on the progress based on the TB model. For a CNT under a magnetic field with strength B, the vector potential is $\mathbf{A} = (\phi/|C_h|, 0)$, where ϕ denotes the magnetic flux threading the CNT. Accordingly, the single-orbital nearest-neighbor TB Hamiltonian is modified by a phase factor,[12]

$$H_j(\mathbf{k}, \phi) = H_j^0(\mathbf{k})\exp(i2\pi\Lambda_i/\phi_0) \qquad (2)$$

where ϕ_0 is the flux quantum and $\Lambda_i = \int_{ri}\mathbf{A} \cdot d\mathbf{r}$. Analytically solving the Hamiltonian yields the electronic spectra of CNTs, $E(\mathbf{k}, \phi)$, which can be used to further calculate the free energy of CNTs by using Fermi–Dirac function. Then, the orbital magnetic susceptibility can be obtained from the second derivative of free energy. This TB model reveals rich magnetic properties for CNTs: (1) Axial magnetic field induces periodic Aharonov-Bohm oscillations in CNT electronic structures, following a metal–insulator transition depending on tube diameter and chirality (Figure 7(a)–(c)). (2) A magnetic field perpendicular to the CNT axis does not change the bandgap, but can cause quantized Landau levels in
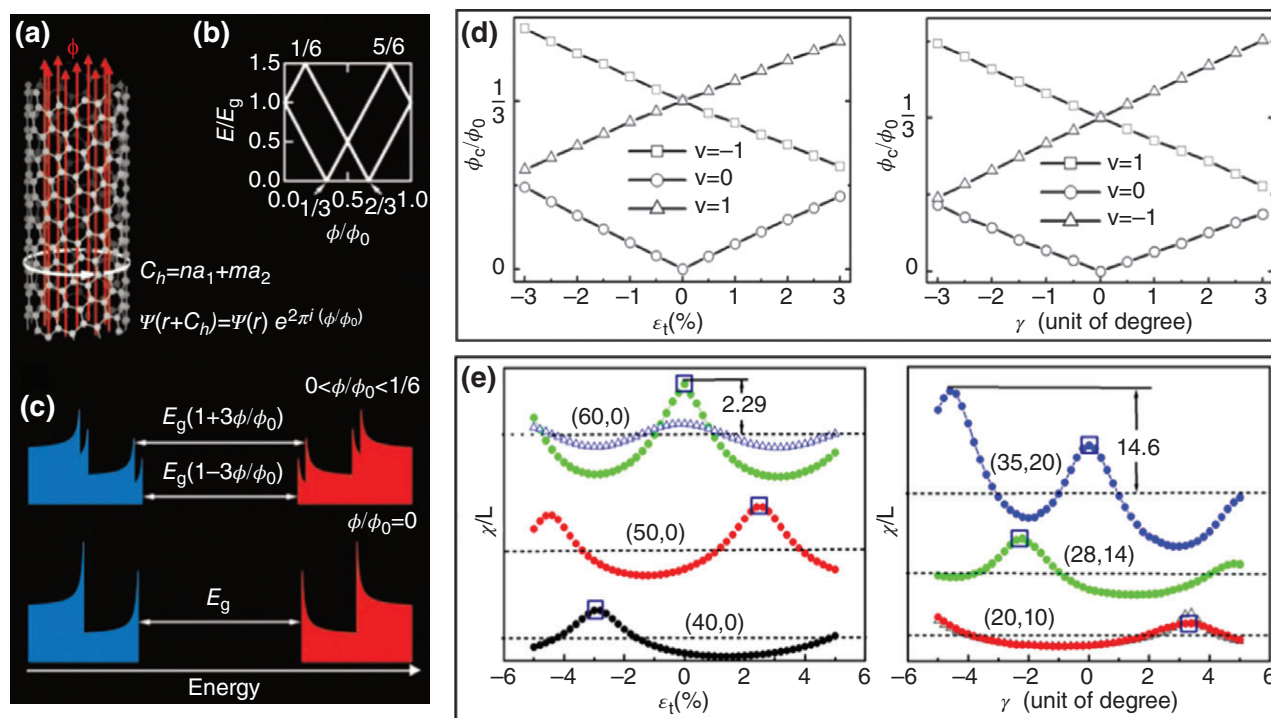
FIGURE 7 | Electromagnetic coupling and mechano-electro-magnetic couping in CNTs. (a) A CNT threaded by a magnetic flux ϕ. (b) The dependence of CNT bandgap on ϕ. The two lines correspond to the gap at K_1 and K_2 points in $\mathbf{k}$ space. (c) Schematic densities of states of the valence (blue) and conduction (red) bands of a CNT with (upper) and without (lower) a magnetic flux. (Reprinted with permission from Ref 89 Copyright 2004 American Association for the Advancement of Science). (d) Critical flux for semiconductor–metal transition as functions of (left) uniaxial and (right) torsional strains. (e) The susceptibility per nanometre of CNTs as a function of (left) uniaxial and (right) torsional strains at temperature of 0 K. Triangles show results at 300 K and the numbers denoting the peak are in unit of 10^{-5} cgs/(mole nm). (Reprinted with permission from Ref 90 Copyright 2007 American Institute of Physics).

the electronic spectra of CNTs. (3) Under an axial magnetic field, metallic CNTs are paramagnetic while semiconducting CNTs are diamagnetic (Figure 7(e)), whereas under the perpendicular magnetic fields all CNTs are diamagnetic; moreover, magnetic susceptibility linearly scales with the tube diameter. These theoretical results well support early transport measurements of CNTs, such as giant magnetoresistance[87] and conductance oscillation[91] under axial magnetic fields. In particular, the periodic magnetic flux modulation of the CNT bandgap has been unambiguously observed independently by Coskun et al.[92] and Zaric et al.[89] from different experimental groups. Note that the conductance oscillation is easier to be observed in MWCNTs, since the oscillating period is $4\phi_0/\pi D$,[2] around several Tesla for a normal MWCNT with $D = 20$ nm.[91] For a SWCNT with D normally being approximately 2 nm, the corresponding period is up to 10^3 Tesla, unattainable in current experiments. However, a beating phenomenon in Aharonov-Bohm type of interference was found to enable effective conductance modulations in SWCNTs under a much smaller magnetic field.[93]

Mechano-Electro-Magnetic Coupling Effect in Carbon Nanotubes

The rich electromechanical and electromagnetic coupling behaviors raise an interesting question regarding how the CNT electronic states are coupled to both strains and magnetic fields. To clarify this issue, Zhang et al.[90] developed a theory based on the TB model by taking into account the uniaxial and torsional strains and magnetic fields. The corresponding Hamiltonian becomes

$$H_j(\mathbf{k},\xi,\phi) = H_j^0(\mathbf{k})\tau_j\left(\exp i\mathbf{k}\bullet\Delta\mathbf{r}_j\right)\exp\left[i(2\pi/\phi_0)\int_{\mathbf{r}_j}\mathbf{A}\bullet d\mathbf{r}\right]$$

(3)

Solving Equation 4, they found strong mechano-electro-magnetic coupling effect in SWCNTs. First, the critical magnetic field required for the metal–insulator transition in CNTs shows a linear yet chirality-dependent modulation with strains (Figure 7 (d)). Second, the susceptibility displays strain-induced

peaks, whose values and distributions rely on both the chirality and tube diameter; interestingly, a switch between paramagnetism and diamagnetism can be realized at certain strain values (Figure 7(e)). Similar analyses have also been carried out by Zhang et al.,[94] who studied the beating of Aharonov-Bohm interference in strained SWCNTs and found that the beating pseudoperiod can be modulated by strain, in a way sensitive to the CNT chirality. Nevertheless, owing to the challenge in concurrently applying strain and magnetic field to CNTs, very limited experimental progress is found in this aspect. Cai et al.[95] measured magnetoresistance of SWCNT bundles under hydrostatic pressure up to 10 GPa and observed a pressure-induced transition in magnetoresistance from positive to negative under high fields, which should be the first evidence of mechano-electro-magnetic coupling effect in CNTs. Strain-tunable magnetic properties of CNTs could open a range of applications, such as pressoelectronic and magnetoelectronic devices.

Contact Effects with Substrates and Electrodes

While CNTs possess a number of exceptional properties in vacuum, the inclusion of CNTs into electronic devices requires integration with substrates, such as dielectric layers, gates and metal contacts. The CNTs can experience massive changes of their properties when put on substrates, posing uncertainty to the performance of CNT-based devices. On the other hand, integrating CNTs and substrates to form hybrid structures may provide properties complementary to those of components. It is thus of both fundamental and technological importance to understand modification of CNT properties by various substrates.

Carbon Nanotube on Metals

In most devices, CNTs need to form contacts with various metal surfaces, such as Pt, Au, Ca, Al and Cu. The properties of CNT devices are found to depend on the contact metals. For example, a semiconducting CNT in field-effect transistors (FETs) exhibits *n*-type properties with Ca electrodes but *p*-type with Pd electrodes.[96] Ballistic *n*-type CNT-based FETs have also been fabricated by contacting semiconducting SWCNTs using Sc or Y, which, combined with the ballistic *p*-type CNT FETs using Pd contacts, enable doping-free fabrication of CNT-based ballistic complementary metal-oxide semiconductor devices.[97] The origin of the doping character of semiconducting SWNTs has been a subject of intensive

debate, and several mechanisms have been proposed for the *p*-type conduction: (1) the doping directly by the contacts,[98] which usually occurs for the metals with high work function, such as Pt; (2) the chemical doping by processing the CNTs in oxidizing acids[99]; (3) the doping by adsorption of atmospheric oxygen.[100] Any of these mechanisms can in principle influence the transistor performance. As for the contact itself, the design of high-performance CNT devices is contingent upon knowing the physics at metal–CNT interfaces, which correlates with the contact area,[101] the metal work function,[102] and the tube diameter and chirality[103] etc. Theoretical analyses on this topic have revealed that the interface conductance scales with contact length, in agreement with an earlier experiment[104]; and an armchair tube couples better than a zigzag tube to ordered Au/Ag contacts.[105] The CNT diameter is another important factor. Both metallic and semiconducting SWCNTs have been demonstrated to form high-quality ohmic contact with Pt, Rh, Pt and Y when the tube diameter is larger than 1.6 nm.[106] For CNTs with diameter smaller than 1.0 nm, ohmic contact proves to be difficult even for metallic CNTs, possibly because small CNTs tend to form stronger CNT-metal bonding that results in larger height of the tunnel barrier at the interfaces. Using large-scale Landauer transport calculations, Nemec et al. revealed that the superiority of Pd is correlated with the nature of CNT-metal interaction, manifested as weak hybridization with a large contact length.[107] Further progress in this area calls for computationally more effective methods that could bridge the gap between experimental and theoretical scales of systems.

Carbon Nanotube on Non-Metal Substrates

The non-metal substrates include insulating and semiconducting substrates. Compared to metal substrates, the non-metal substrates often have less charge exchange with CNTs. On insulating substrates, such as SiO_2 and h-BN, CNTs have little change in electronics, except for possible radial deformation induced by substrate adsorption.[108] Some interesting behaviors can arise in CNTs adsorbed on semiconducting substrates, on which the electronic properties of CNTs are sensitive to local chemical environments. First-principles calculations showed that armchair CNTs can be chemisorbed on clean Si(001) via the formation of Si–C bonds, which enhance the metallic character of the nanotubes.[109] In another work, the CNTs on Si(001) were shown to have different favorable adsorption sites depending on the nanotube directions and the local

substrate geometry, entailing distinctly different electronic structures to the CNTs.[110,111] Zigzag CNTs were also predicted to strongly adsorb on InAs, primarily by the hybridization between the carbon π orbitals and cation dangling-bonds of substrate; differently aligned CNTs on nonpolar InAs surfaces form almost the same band alignment while on polar surfaces the CNTs can be auto-doped into *n* or *p* type due to large surface dipoles,[112] suggesting that CNTs can acquire richer functionalities on binary substrates. Integrating CNTs with semiconductor surfaces will inherit huge expertise from current semiconductor technology and will benefit the development of nanoscale hybrid electronic and optoelectronic devices.

## GRAPHENE-LIKE NANOSTRUCTURES

h-BN Nanostructures

Monolayer h-BN sheet is an isostructural and isoelectronic analogue to graphene, and could serve as an excellent substrate for high-performance graphene electronics.[113] Scalable growth of quality h-BN monolayers has been achieved through chemical vapor deposition on a range of substrates.[114–116] The h-BN monolayer is featured by its bond ionicity, which localizes the electronic states and results in enhanced chemical and thermal stabilities. Thus, h-BN sheet shows unique potential of fabricating nanoscale devices operable in harsh environments. On the other hand, the bond ionicity breaks the symmetry of electronic states and opens a large bandgap near the Fermi level, rendering all h-BN nanostructures electrically insulating. The insulating properties severely hinder the applications of h-BN in functional devices. Extensive research efforts have been devoted to modifying the electronic properties of h-BN nanostructures, in particular those of nanotubes and nanoribbons.

Boron Nitride Nanotubes

BN nanotubes (BNNTs) are isostructural to CNTs.[117,118] Mechanically, BNNTs possess excellent mechanical properties with a Young's modulus up to 0.7 TPa[119] as well as superb yield strength against axial tension.[120,121] Electronically, the BNNTs remain insulating with a bandgap approximately 5.5 eV independent of the tube chirality, in contrast to CNTs. Another unique feature is that most BNNTs are in zigzag type because of the preference of aligning tube axes along the (1010) direction of h-BN during synthesis.[122] When the tube diameter is less than 0.95 nm, strong rehybridization effect can rapidly reduce the bandgap of zigzag BNNTs with decreasing diameter.[123] Moreover, zigzag BNNTs experience an axial deformation approximately 1% under an applied external electric field of 1 V/Å, attributed to both electrostrictive effect and converse piezoelectric effect, and the deformation ratio increases with decreasing tube diameter.[124] In recent years, the interest of pushing BNNTs toward electronic applications has been boosted by a variety of methods of tuning their insulating bandgap. Mechanically, Kim et al., found that a radial deformation at a transverse pressure of about 10 GPa can decrease the bandgap of zigzag BNNTs down to 2 eV,[125] due to the downshift of π^* states. Electrically, the bandgap of BNNTs can be significantly reduced by transverse electric fields[126,127] and the gap modulation is more notable with increasing the tube diameter, showing a giant Stark effect as confirmed in subsequent experiment.[128] The bandgap modulation in BNNTs by strain or electric field is superior to that by means of chemical routes, such as dopants[129] or functionalizations,[130] in a sense that the latter incurs localized states detrimental to device performance. Chemically, fluorination proves to be effective to enrich the functionalities of BNNTs, such as inducing *p*-type doping[129] and long-ranged ferromagnetic spin ordering that is even tunable by radial deformation.[131]

The experimentally synthesized BNNTs tend to be multiwalled, mostly even walls.[132] The interwall interaction can significantly affect the electronic properties of multiwalled BNNTs. For example, the bandgap of a multiwalled BNNT is found to be remarkably narrower than any of its single-walled constituents; the valence band maximum (VBM) and conduction band minimum (CBM) are distributed on the outermost and innermost tubes, respectively.[133] Thus, the multiwalled BNNTs can serve as a coaxial semiconductor junction with type II band alignment across the radial direction. Zhang et al. predicted that the band alignment between the inner and outer walls of a double-walled BNNT can be tuned from type II to type I by radial deformation, following a direct to indirect bandgap transition and a substantial gap reduction[134]; moreover, the bandgap of a squashed double-walled BNNT can be further significantly reduced by a transverse electric field. Zhang et al. further showed that small double-walled BNNTs could be natural homogeneous nanocables as injected electrons prefer abnormally to concentrate on the inner wall while the outer wall keeps electrically neutral, breaking the tradition of heterogeneous coaxial structures for common cables.[135]
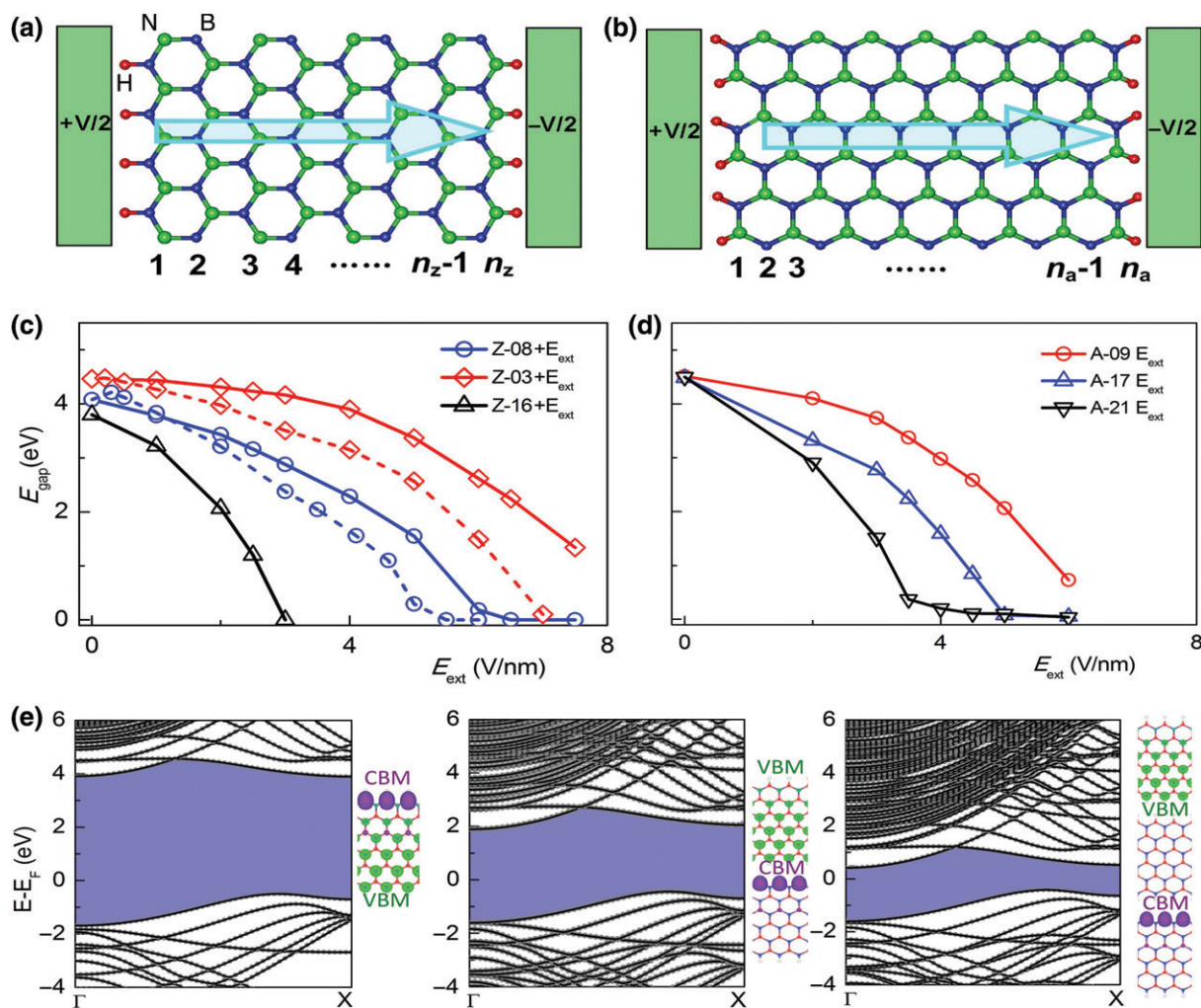
FIGURE 8 | Tunable electronic properties of BN nanoribbons. (a,b) Atomic structures of (a) zigzag and (b) armchair nanoribbons, with widths of $n_z = 8$ and $n_a = 15$, respectively. (c,d) Bandgap as a function of field strength for the (c) zigzag and (d) armchair nanoribons. Dot lines in (c) are for the modulation under reversed electric field (pointing from the N edge to the B edge). (Reprinted with permission from Ref 4 Copyright 2008 American Physical Society). (e) Band structures and partial charge densities (0.006 e/Å^3) for the VBM (green) and CBM (violet) in aligned zigzag nanoribbons with different ribbon numbers. (Reprinted with permission from Ref 136 Copyright 2013 Royal Society of Chemistry).

BN Nanoribbons

BNNRs have also been the focus of much research attention (see Figure 8(a) and (b) for structures). BNNRs can be synthesized with high quality by longitudinal splitting of BNNTs[137] or by morphology control of metal catalysts during chemical vapor deposition.[138] The BNNRs with standard armchair (A-BNNRs) and zigzag edges (Z-BNNRs) are of particular interests. Without edge passivation, the A-BNNRs are nonmagnetic semiconductors while the Z-BNNRs have a magnetic ground state with extended spin ordering along the edges. With hydrogen passivation, all BNNRs become nonmagnetic insulators[4]; the Z-BNNRs have decreased bandgap with increasing ribbon width due to enhanced

transverse electric polarization. In the past few years, extensive theoretical efforts have been devoted to narrowing the bandgap of hydrogen-passivated BNNRs. Zhang et al. showed for the first time that the bandgap of BNNRs can be reduced by applying transverse electric fields, resulting in giant Stark effect due to reduced electric field screening[4]; it is of practical importance that the gap modulation is more sensitive in a wider BNNR (Figure 8(c)–(d)). Later on, similar results were reported for large-width BNNRs by Louie et al.[139] External electric fields could also couple with the spin ordering along the edges of bare BNNRs, giving rise to magnetic metal–semiconductor-half-metal transitions.[140] However, the field strength required for desirable bandgap modulation

reaches the level of V/nm, which remains too strong for practical application. Alternatively, introducing impurity states into the BNNRs by either chemical decoration at the edges or defect engineering proves to be an effective way. The Z-BNNRs can be functionalized into metallic, magnetic and even half-metallic materials by partial hydrogenation,[141] or embedding line defects[142,143] or edge attachment of oxygen or sulfur atoms.[144] However, manufacturing these functionalized BNNRs still requires sophisticated fabrication processes which render the demand for mass production impractical. Also, the bandgap of both A- and Z-BNNRs can be effectively modulated by uniaxial strain.[145,146] In particular, the spontaneous electric polarization in Z-BNNRs can strongly couple with the elastic strain, offering not only more sensitive strain modulation in a wider ribbon but also a novel piezoelectric behavior.

Functional BN Nanostructures

Given the experimental subtlety in realizing strong electric field and mechanical strain, a concept of intrinsic Stark effect induced by built-in electric polarization was demonstrated by Zhang et al. to spontaneously tune cubic BN nanofilms into semiconductor and even metal.[147] Using hybrid DFT calculations with van der Waals correction, Zhang et al. further showed that polar BNNRs can be favorably aligned edge-by-edge via substantial hydrogen bonding at the interfaces,[136] which induces significant interface polarizations and sharply reduces the bandgap of BNNRs well below silicon range (Figure 8(e)). Chemically, fluorination could transform a h-BN multilayer into a semiconducting c-BN nanofilm, which possesses substantial ferromagnetism upon electron doping.[148] Substrates also modify the intrinsic properties of h-BN sheet in a significant way. It was predicted that an oxidized h-BN sheet supported on Cu substrate exhibits metallic properties when O adatoms vertically bond with B atoms.[149] Further study showed that, upon chemisorption of ozone molecules or O-H groups on B atoms, the h-BN sheet on Cu exhibits ferromagnetic, antiferromagnetic or ferrimagnetic ordering depending on the adsorption density and configuration of functional groups.[150]

Metal Dichalcogenide Nanostructures

As one of inorganic analogues of graphene, single-layer transition metal dichalcogenides (TMDs) MX_2 (M=Mo, W, Ta, Sc, Ti, V, Cr, Mn, Fe, Co, Ni, Nb; X=S, Se, Te) have sparked tremendous research interest as they can be superior to graphene in certain respects (also summarized in recent reviews[151,152]). Of particular interest is the MoS_2 monolayer, in which one Mo layer is sandwiched between two S layers in a trigonal prismatic lattice (Figure 9(a)). The crystal field splitting of Mo d orbitals combined with reduced dimensionality yields a direct bandgap of 1.8 eV at the K point (Figure 9(d)),[156] which is desirable for fabricating FETs, photo detectors, photoelectronic devices. In contrast, few-layer and bulk MoS_2 have indirect bandgap, with the VBM at the Γ point and CBM at a point in the Γ-K path.[157] The direct–indirect transition is believed to stem from the interlayer van der Waals interaction.[156,158]

In-Plane Strain Effect

Electronic structures of monolayer or few-layer MoS_2 are very sensitive to elastic strains, which can be realized by putting MoS_2 samples on a flexible substrate and then deforming the substrates, or directly on a piezoelectric substrate (Figure 9(b) and (c)).[153,154] Among different forms of strains, the biaxial strain is most effective for tuning the bandgap. For monolayer MoS_2, DFT studies showed that a direct-to-indirect bandgap transition can occur at a biaxial tensile strain of approximately 1% (Figure 9 (e)), as a result of the downshift of the topmost valence band at the K point with respect to that at the Γ point.[155,159] Meanwhile, as shown in Figure 9 (e), both the direct gap at the K point and the indirect bandgap between the K and Γ points are reduced, caused by the rapid downshift of the CBM. Further, the monolayer MoS_2 can become metallic at a biaxial tensile strain over 10% or compressive strain over 15%.[160] Tensile strain could also enhance the carrier mobility in monolayer MoS_2 by increasing the band dispersion. Applied uniaxial tensile and shear strains also dramatically reduce the bandgap of monolayer MoS_2.[161] For few-layer MoS_2, photoluminescence spectra revealed that the bandgap decreases by 120 meV per 1% uniaxial tensile strain in bilayer MoS_2[153] and increases by approximately 300 meV per 1% biaxial compressive strain in trilayer MoS_2.[154] It appears that the strain-tunable bandgap is more sensitive in thicker MoS_2 layers, thanks to the coupled effect of the in-plane strain and the out-of-plane deformation due to the Poisson effect. Moreover, biaxial compressive strain causes a significant increase of photoluminescence intensity in trilayer MoS_2.[154]

Out-of-Plane Strain Effect

We now discuss the effect of out-of-plane strain. Dou et al. detected that under hydrostatic pressure the optical transition of a bilayer MoS_2 changes from
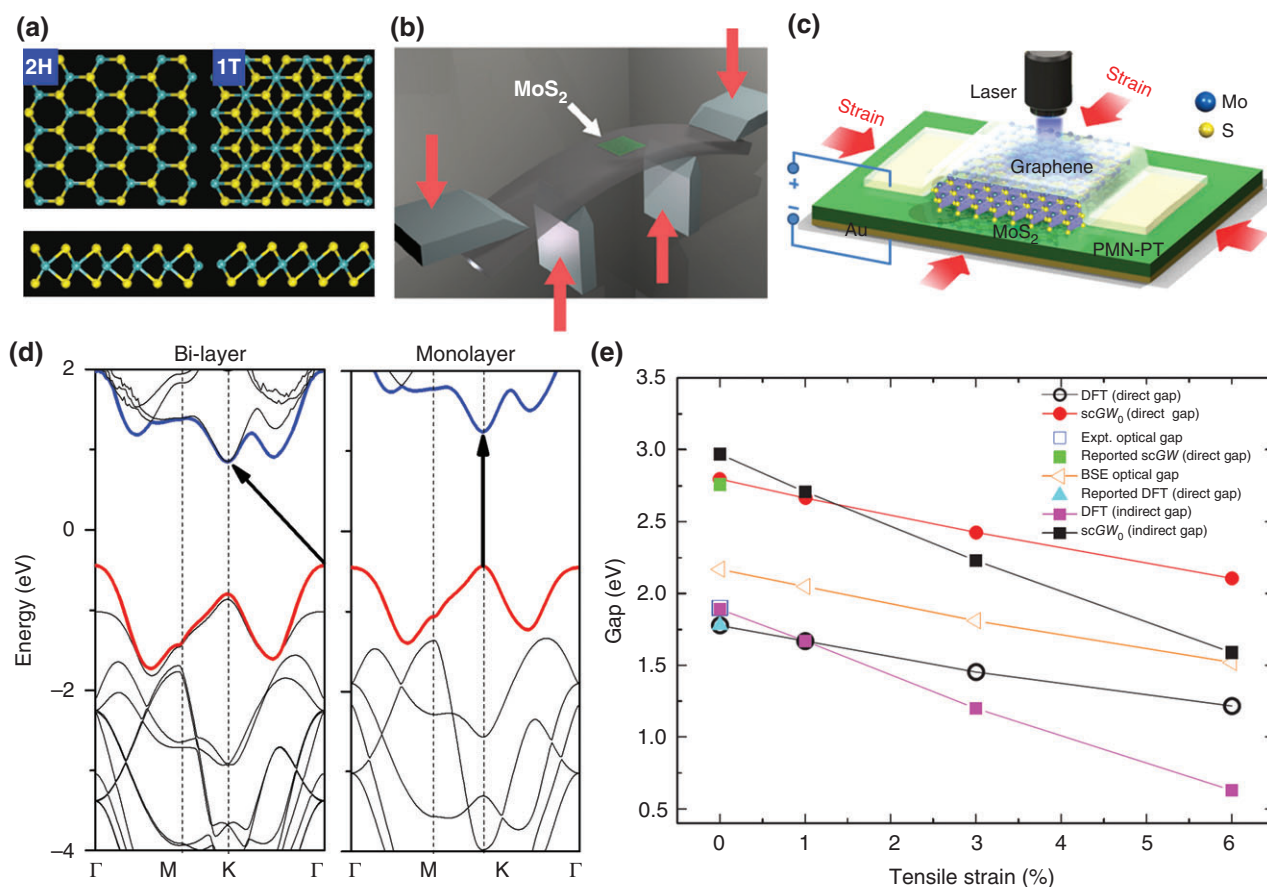
FIGURE 9 | Electronic structures and strain engineering of MoS$_2$. (a) Atomic structures of monolayer MoS$_2$ in 2H and 1 T phases. (b) The loading strategy of experimental realization of uniaxial tensile strain in 2D MoS$_2$. (Reprinted with permission from Ref 153 Copyright 2013 American Chemical Society). (c) The loading strategy of realizing biaxial compressive strain by a piezoelectric substrate. (Reprinted with permission from Ref 154 Copyright 2013 American Chemical Society). (d) Band structures of bi- and mono-layer MoS$_2$. (e) Calculated direct and indirect bandgaps in monolayer MoS$_2$ as a function of biaxial strain. (Reprinted with permission from Ref 155 Copyright 2013 American Physical Society).

direct (K-K) to indirect (Λ-K), due to a changeover of the CBM from the K point to the Λ point.[162] Peña-Álvarez observed that under vertical compression the monolayer MoS$_2$ experiences a direct-to-indirect gap transition at 0.5 GPa and ends up with semimetal at 3 GPa.[163] Hydrostatic pressure could also induce a semiconductor–metal transition in multilayer MoS$_2$ due to an overlap of valence and conduction bands as the interlayer distance decreases.[164,165] In contrast, Tongay et al. found that the interlayer interactions in few-layer MoSe$_2$ can be weakened by thermal expansion, which leads the system properties close to the limit of monolayer.[166]

Magnetic 2D TMDs

As mentioned, 2D TMDs can also exist as MX$_2$ with M=Sc, Ti, V, Cr, Mn, Fe, Ni, Nb, W, Ta, Sn and X=S, Se. These TMDs have lattice structures similar to MoS$_2$. Specifically, the CrS$_2$, CrSe$_2$, FeS$_2$, FeSe$_2$, MoS$_2$, MoSe$_2$, WS$_2$, WSe$_2$, TaS$_2$ and TaSe$_2$ energetically favor the 2H phase, while TiS$_2$, TiSe$_2$, MnS$_2$, MnSe$_2$, NbS$_2$, SnSe$_2$ and SnS$_2$ favorably adopt the 1-T phase (see Figure 9(a), right); whereas the ScS$_2$, ScSe$_2$, VS$_2$, VSe$_2$, CoS$_2$, CoSe$_2$, NiS$_2$, NiSe$_2$ and NbSe$_2$ can be stable in both phases with competitive stability.[167] The subgroup of 2D MX$_2$ with M=Mo, W and X=S, Se are very similar to the 2D MoS$_2$ in terms of lattice and electronic structures; the rest can exhibit distinct properties, such as magnetism. Straining 2D magnetic TMD monolayers could weaken the metal-ligand bonding and localize metallic electronic states therein. This will change the exchange interaction between local spin moments and result in remarkable mechano-magnetic coupling. Ab initio study showed that the magnetism in the 2D VSe$_2$ monolayer can be enhanced by applying a biaxial tensile strain,[168] and the ferromagnetic ordering is robust against deformation. In contrast, the ground state of 2D NbSe$_2$ can be switched from antiferromagnetic to ferromagnetic when a biaxial
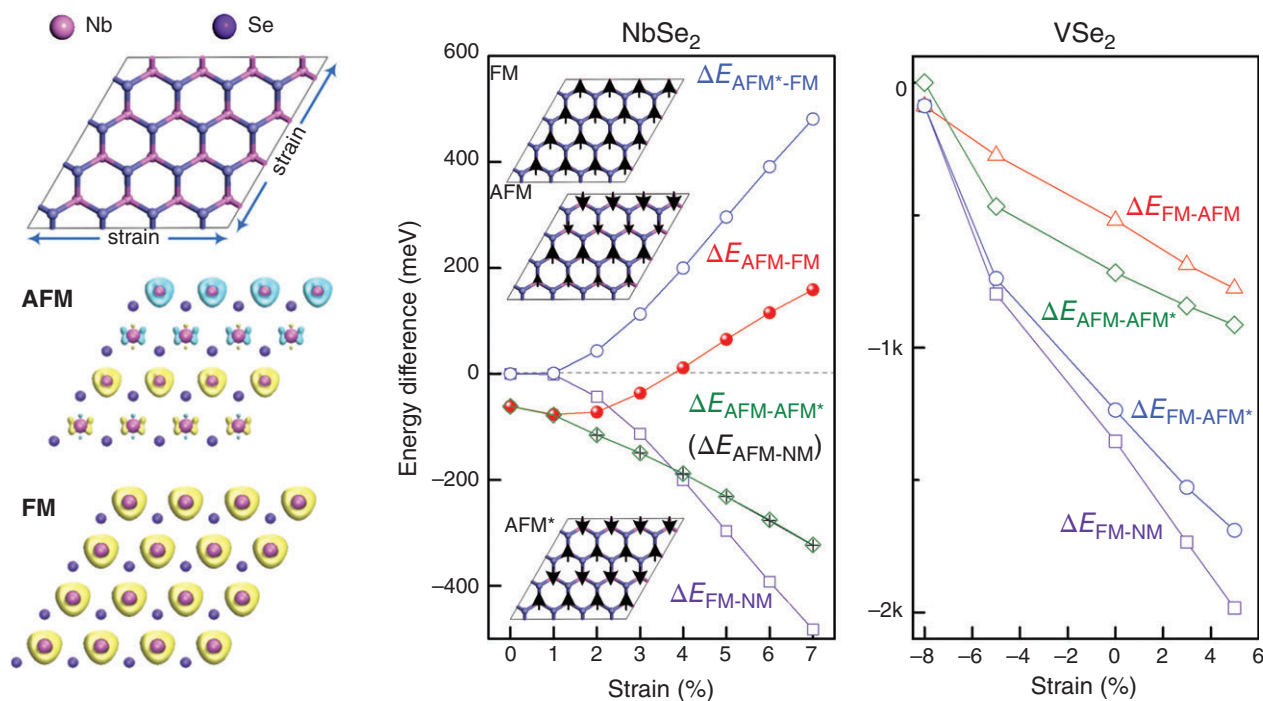
FIGURE 10 | Strain-tunable magnetism in monolayer $NbSe_2$ and VSe_2. Left panel: atomic geometry of monolayer $NbSe_2$ and isosurface plots (0.05 e/$Å^3$) of magnetization densities for the antiferromagnetic and ferromagnetic states. Right panel: relative stability of different magnetic orderings in the $NbSe_2$ and VSe_2 monolayers as functions of biaxial strain. (Reprinted with permission from Ref 169 Copyright 2014 Royal Society of Chemistry).

tensile strain over 4% is applied,[169] as energetically reflected in Figure 10 by energy. Also, a biaxial strain over 6% switches the ground state of 2D TaS_2 and $TaSe_2$ from Pauli-paramagnetic to ferromagnetic.[170] Both $SnSe_2$ and SnS_2 monolayers are semiconducting with indirect bandgaps, which can be closed under an applied biaxial strain of approximately 10%.[171]

Currently, experimental progress of fabricating the 2D TMDs is advancing rapidly, and the syntheses of 2D WS_2, WSe_2, VS_2, $NbSe_2$, $TaSe_2$, $NbSe_2$ and $NiTe_2$ have been reported successively.[172–175] Unfortunately, the reports of magnetism in these 2D TMDs are very few, possibly because the synthesized samples are not sufficiently thin. So far, only the ultrathin VS_2 nanosheets was reported to be ferromagnetic by Gao et al.,[173] and all other magnetic 2D TMDs remain to be confirmed by dedicated experiments.

Phosphorene Nanostructures

Phosphorene, a monolayer of black phosphorus, has been a rising star material since the first demonstration of using it for fabricating high performance FETs.[176,177] In contrast to the honeycomb lattice of graphene, h-BN and TMDs, the lower-symmetry puckered structure of phosphorene (Figure 11(a)) leads to superior mechanical flexibility[180] and

anisotropic electronics.[181,182] The band structure of phosphorene shows direction-dependent dispersion near the Fermi level (Figure 11(b)), giving rise to anisotropic electric conductance and carrier mobility.[178]

Structural flexibility of phosphorene offers a great opportunity to tune its electronic properties by elastic strain. Theoretically, a single-layer phosphorene can withstand a tensile stress and strain up to 10 N/m and 30%, respectively.[183] The electronic states near the band gap show different distributions in their wave function, so that they response differently to strain (Figure 11(b)), leading to an effective modulation of the conductance anisotropy. For instance, a moderate biaxial or uniaxial strain (4–6%) causes a 90° rotation of the preferred conducting direction, as supported by the change of electron effective mass shown in Figure 11(c),[178] which is attributed to the changeover of the lowest conduction bands with different anisotropic dispersions (Figure 11(b)). Regarding the bandgap, biaxial compressive strain decreases the gap value and induces a semiconductor–metal transition at −9% strain; whereas biaxial tensile strain first increases the gap to a peak at 4% strain and decreases it thereafter (Figure 11(d)),[179] just as a result of the preceding changeover of the lowest conduction band at 4% strain. Upon applying a uniaxial strain, the bandgap
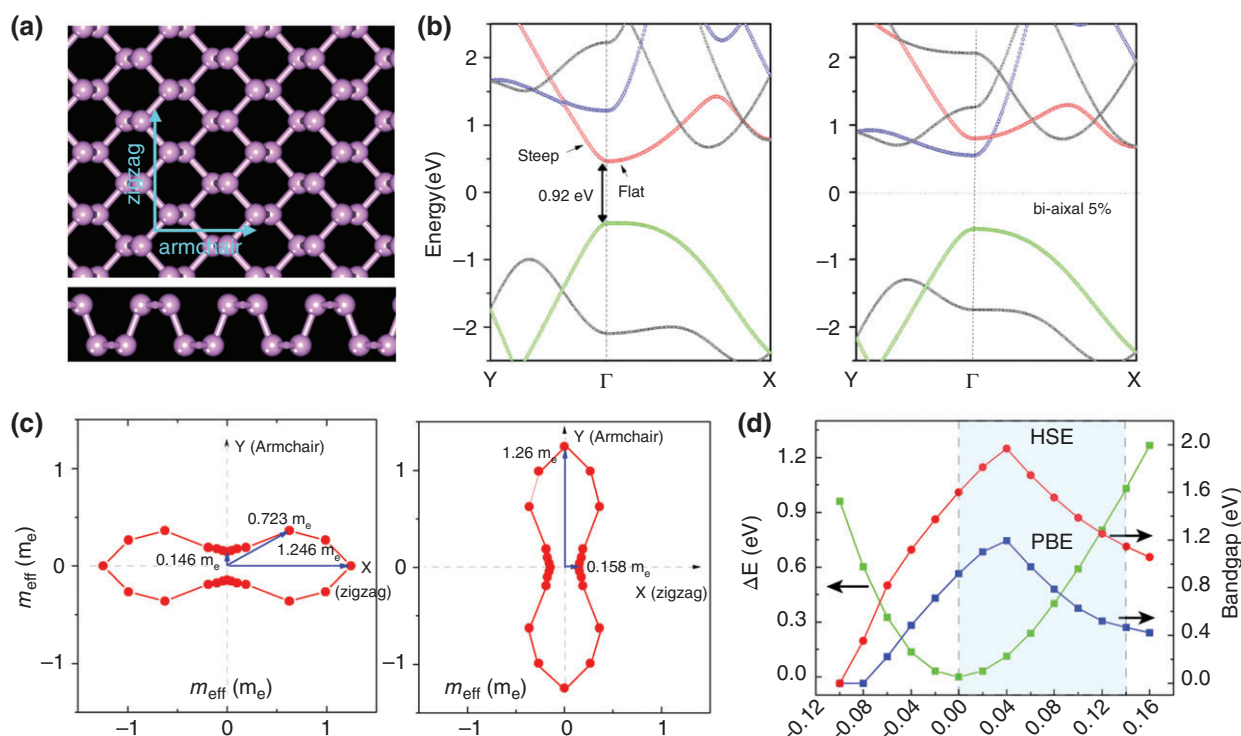
FIGURE 11 | Geometry structure and intrinsic anisotropy of phosphorene. (a) Atomic structure in the top and side views. (b) Band structures of monolayer phosphorene under (left) 0 and (right) 5% biaxial tensile strains, where the bands along the Γ-X and Γ-Y directions have anisotropic dispersion. (c) Direction-dependent electron effective mass of phosphorene under (left) 0 and (right) 5% biaxial tensile strains. (Reprinted with permission from Ref 178 Copyright 2014 American Chemical Society) (d) Bandgap and strain energy ΔE of phosphorene as functions of the biaxial strain. (Reprinted with permission from Ref 179 Copyright 2014 American Chemical Society).

of phosphorene can experience a direct–indirect–direct transition; moreover, the conduction band extreme converges at some critical strain, yielding enhanced thermoelectric performance.[184]

In addition to strain, external electric fields have also been adopted to tune the electronic properties of phosphorene. A recent theoretical study revealed a Stark effect in phosphorene under electric fields applied along the normal of the basal plane, showing continuous gap modulation.[179] In few-layer phosphorene, applied vertical electric field leads to even richer functionalities as increasing field strength not only decreases the bandgap but induces a transition from normal insulator to topological insulator and finally to metal.[185]

Research attention has also been paid to phosphorene nanoribbons, nanotubes and van der Waals multilayers. Both armchair and zigzag phosphorene nanoribbons with H-passivated edges inherit the semiconducting nature of phosphorene, and their bandgaps depend on the ribbon width w.[186] The bandgap of the armchair phosphorene nanoribbon scales as $1/w^2$, while that of the zigzag phosphorene nanoribbon exhibits a $1/w^2$ behavior.[187] As for the

multilayers, bilayer phosphorene under a small vertical compression exhibits a high electron mobility of 7×10^4 cm^2 V^{-1} s^{-1} at room temperature as a result of a newly emerged conduction band extreme.[188]

Other Newly Emerged 2D Material and Related Nanostructures

All above 2D materials are naturally lamellar in their bulk forms, with the component layers assembled by van der Waals interaction. Recently, the research enthusiasm on 2D materials has been extended to those, whose bulk forms are not layered in nature. These 2D materials include hexagonal MXenes, silicene, germanene, ZnO sheets and tetragonal TiC monolayer, etc, which need special conditions for stabilization, such as structural buckling, chemical passivation and support on substrates.

MXenes

MXenes can be obtained by etching out the A layers from MAX materials at room temperature, where M is an early transition metal, A can be a group IIIA or IVA element, X is C and/or N.[189] The MXene family
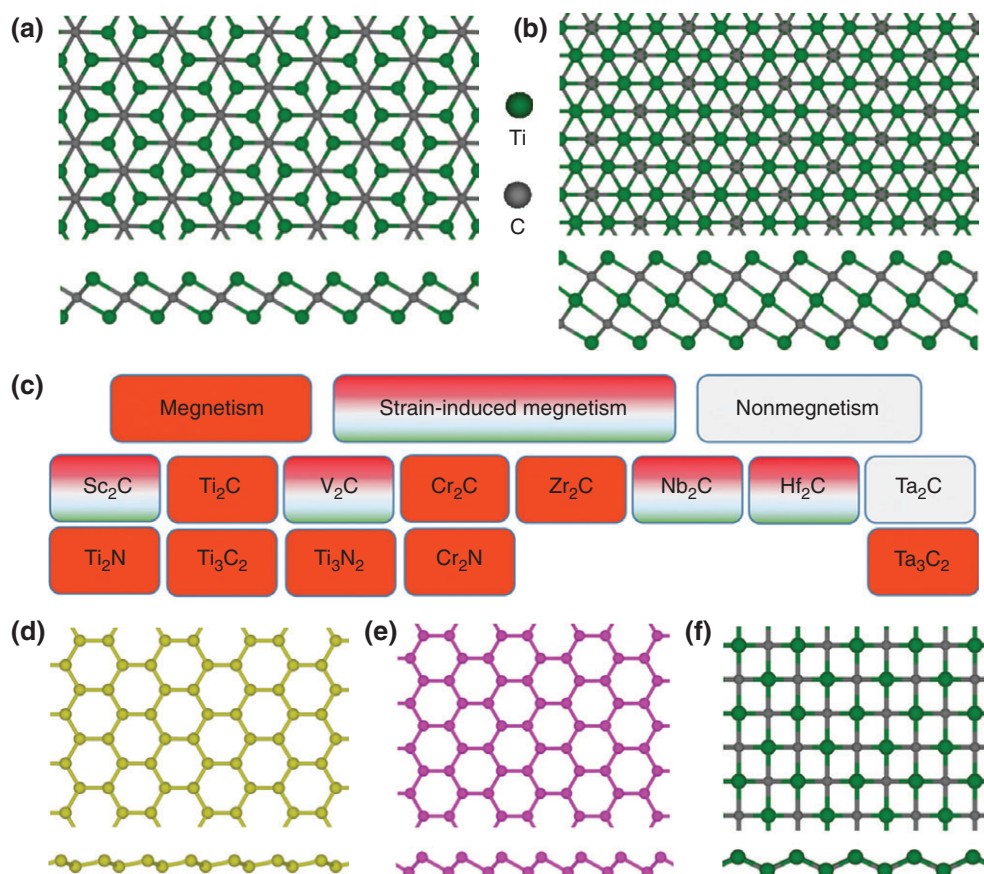
FIGURE 12 | Other newly emerged 2D materials. (a,b) Front and side views of atomic structures of 2D (a) Ti_2C and (b) Ti_3C_2. (c) A map of magnetic 2D MXenes. (d–f) Front and side views of atomic structures of 2D (d) silicene, (e) arsenene and (f) TiC monolayers.

includes 2D Ti_2C (Figure 12(a)), Ti_3C_2 (Figure 12 (b)), Nb_2C, V_2C, $(Ti_{0.5},Nb_{0.5})_2C$, $(V_{0.5},Cr_{0.5})_3C_2$, Ti_3CN and Ta_4C_3. All bare MXene monolayers are terminated by M layers and therefore are strongly metallic, with a high electron density of states near the Fermi level. Chemical passivation of MXenes surfaces eliminates the metallic states and results in 2D semiconductors[190] and even topological insulator.[191] Very recently, the 2D Sc_2CF_2 is fabricated and used to construct vdW heterostructures with the MoS_2 monolayer, whose electronic structure turns out to be extremely sensitive to in-plane biaxial strain: a ~1.5% tensile strain suffices to induce an insulator-metal transition.[192]

While most MXenes are non-magnetic, the 2D Cr_2C, Cr_2N, or Ta_3C_2 are ferromagnetic and the 2D Ti_3C_2 and Ti_3N_2 are antiferromagnetic (Figure 12 (c)). Like magnetic TMDs, these MXenes have tunable magnetism by in-plane strain as well. The intrinsic magnetic moments of 2D Ti_2C and Zr_2C are 1.92 and 1.25 μ_B per primitive cell, which can be enhanced by 11.5 and 60% under biaxial tensile

strains of ~8 and 3%, respectively.[193] For 2D M_2C (M=Hf, Nb, Sc, Ta, V), their nonmagnetic ground state can be switched to ferromagnetic one by tensile strain, with the critical strain for the switch depending on M. These results, together with those of magnetic 2D TMDs, feature a universal behavior of tailoring the magnetism of 2D materials by engineering strain.

Silicene and Silicene-Like 2D Materials

Silicene (Figure 12(d)), germanene, arsenene (Figure 12(e)) and antimonene are a group of 2D materials with honeycomb lattice yet out-of-plane structural buckling. Silicene, the silicon analogue of graphene, is a gapless semimetal with a Dirac cone in its band dispersion[194] and can open a bandgap that is linearly tunable by an applied vertical electric field.[195] While the synthesis of silicene has been reported for several years, its transfer from catalytic metal substrates for fabricating FETs was demonstrated until recently.[196]

In contrast, arsenene and antimonene are semiconductors with indirect bandgaps of 2.49 and 2.28 eV, respectively.[197] Applied tensile strain can sensitively modulate the bandgaps of arsenene and antimonene from indirect to direct, accompanying with a substantial bandgap reduction in the arsenene.

2D ZnO Monolayer

When a ZnO (0001) nanofilm is only a few ZnO layers thin, it prefers a planar configuration, like the h-BN sheet, driven by the disappeared surface dipole. A monolayer of such ZnO sheet can be shaped into nanoribbons, whose electronic properties are unusual due to peculiar edge states[198] and are tunable by external electric fields[199] and edge passivations with hydrogen.[200] In particular, bare zigzag ZnO nanoribbons exhibit edge magnetism that can be remarkably modulated and even completely quenched by applied transverse fields, depending on the field direction.

Beyond the hexagonal 2D materials, Zhang et al. predicted a 2D tetragonal TiC (Figure 12(f)) monolayer sheet with zigzag-shaped buckling structure, which possesses anisotropic electronic properties and an indirect bandgap of 0.21 eV, thus promising for applications in nanoelectronics.[201]

CONCLUDING REMARKS

We have comprehensively reviewed the progress on tunable electronic and magnetic properties of low-dimensional materials, with focus on the modulation by external electric field, strain and substrates. In spite of the significant difficulties in applying the electric fields and nanoscale strain and in performing related analyses and characterizations, notable breakthroughs in realization of tunable properties in different low-dimensional materials have recently been achieved within several experimental groups. Fully delivering these useful properties into applications remains contingent upon the development of advanced fabrication technology, especially the ability to reliably and repeatedly handle the modulation. On the theoretical side, the main challenge is to develop new and/or optimize existing and promising

principles governing the tunable properties as well as to demonstrate their transferability and sometimes preferable applications when integrating the nanomaterials into a device system. For example, for one-dimensional layered materials, applied electric field vertical to the basal plane is more compatible with current device basis than the transverse fields, as recently demonstrated for realizing half-metal in GNRs.[35] Moreover, instead of applying strong external electric fields, using the built-in electric fields in materials or at the interfaces is another direction deserving further attention; yet how the built-in electric fields can be effectively manipulated remains an open question. On the other hand, to take full advantage of the strain effect in low-dimensional materials, it is important to explore innovative technologies that can enhance the strain sensitivity and that enable the operation of strain in a cost-effective and technically feasible way. Moreover, whether there is a theory capable of describing the nanoscale strain–functionality relationship, just as an extended version of conventional stain–stress relationship in continuum, is also an appealing question.

Aside from the mechano-electro-magnetic coupling, the coupling effects induced by various fields in low-dimensional materials can be extended into a broader spectrum, which includes opto-electronic, magneto-optical, thermo-optical and photo-acoustic couplings etc. Having all the atoms exposed on the surfaces, the low-dimensional materials have become an important platform for exploring these peculiar couplings with high sensitivity and efficiency toward manipulating their intrinsic properties and developing novel applications. For example, the two-dimensional MoS_2 monolayer, with inherent spin-orbit coupling and inversion symmetry, has the valley and spin inherently coupled to enable control of valley polarization by optical pumping with circularly polarized light,[202,203] which opens the door for developing integrated valleytronic and spintronic applications. While detailed discussion of these aspects is beyond the focus of this report, they are all promising research directions for realizing the full potential of low-dimensional materials.

REFERENCES

1. Baughman RH, Zakhidov AA, de Heer WA. Carbon nanotubes – the route toward applications. *Science* 2002, 297:787–792.

2. Guo W, Guo Y, Zhang Z, Wang L. Strength, plasticity, interlayer interactions and phase transition of low-dimensional nanomaterials under multiple fields. *Acta Mech Solid Sin* 2012, 25:221–243.

3. Novoselov KS, Geim AK, Morozov SV, Jiang D, Katsnelson MI, Grigorieva IV, Dubonos SV, Firsov AA. Two-dimensional gas of massless Dirac fermions in graphene. *Nature* 2005, 438:197–200.

4. Zhang Z, Guo W. Energy-gap modulation of BN ribbons by transverse electric fields: first-principles calculations. *Phys Rev B* 2008, 77:075403.

5. Geim AK, Novoselov KS. The rise of graphene. *Nat Mater* 2007, 6:183–191.

6. Li X, Wang X, Zhang L, Lee S, Dai H. Chemically derived, ultrasmooth graphene nanoribbon semiconductors. *Science* 2008, 319:1229–1232.

7. Son Y-W, Cohen ML, Louie SG. Energy gaps in graphene nanoribbons. *Phys Rev Lett* 2006, 97:216803.

8. Hod O, Barone V, Peralta JE, Scuseria GE. Enhanced half-metallicity in edge-oxidized zigzag graphene nanoribbons. *Nano Lett* 2007, 7:2295–2299.

9. Liang X, Jung Y-S, Wu S, Ismach A, Olynick DL, Cabrini S, Bokor J. Formation of bandgap and subbands in graphene nanomeshes with sub-10 nm ribbon width fabricated via nanoimprint lithography. *Nano Lett* 2010, 10:2454–2460.

10. Pedersen TG, Flindt C, Pedersen J, Mortensen NA, Jauho A-P, Pedersen K. Graphene antidot lattices: designed defects and spin qubits. *Phys Rev Lett* 2008, 100:136804.

11. Liu X, Zhang Z, Guo W. Universal rule on chirality-dependent bandgaps in graphene antidot lattices. *Small* 2013, 9:1405–1410.

12. Lu JP. Novel magnetic properties of carbon nanotubes. *Phys Rev Lett* 1995, 74:1123.

13. Zhou SY, Gweon GH, Fedorov AV, First PN, De Heer WA, Lee DH, Guinea F, Neto AHC, Lanzara A. Substrate-induced bandgap opening in epitaxial graphene. *Nat Mater* 2007, 6:770–775.

14. Castro EV, Novoselov KS, Morozov SV, Peres NMR, Dos Santos JMBL, Nilsson J, Guinea F, Geim AK, Neto AHC. Biased bilayer graphene: semiconductor with a gap tunable by the electric field effect. *Phys Rev Lett* 2007, 99:216802.

15. Zhang Y, Tan Y-W, Stormer HL, Kim P. Experimental observation of the quantum Hall effect and Berry's phase in graphene. *Nature* 2005, 438:201–204.

16. Novoselov KS, Jiang Z, Zhang Y, Morozov S, Stormer H, Zeitler U, Maan J, Boebinger G, Kim P, Geim A. Room-temperature quantum Hall effect in graphene. *Science* 2007, 315:1379.

17. Goerbig MO. Electronic properties of graphene in a strong magnetic field. *Rev Mod Phys* 2011, 83:1193.

18. Guinea F, Katsnelson M, Geim A. Energy gaps and a zero-field quantum Hall effect in graphene by strain engineering. *Nat Phys* 2010, 6:30–33.

19. Zhang D-B, Seifert G, Chang K. Strain-induced pseudomagnetic fields in twisted graphene nanoribbons. *Phys Rev Lett* 2014, 112:096805.

20. Levy N, Burke S, Meaker K, Panlasigui M, Zettl A, Guinea F, Neto AC, Crommie M. Strain-induced pseudo–magnetic fields greater than 300 tesla in graphene nanobubbles. *Science* 2010, 329:544–547.

21. Choi S-M, Jhi S-H, Son Y-W. Effects of strain on electronic properties of graphene. *Phys Rev B* 2010, 81:081407.

22. Cocco G, Cadelano E, Colombo L. Gap opening in graphene by shear strain. *Phys Rev B* 2010, 81:241412(R).

23. McCann E. Asymmetry gap in the electronic band structure of bilayer graphene. *Phys Rev B* 2006, 74:161403.

24. Yan K, Peng H, Zhou Y, Li H, Liu Z. Formation of bilayer bernal graphene: layer-by-layer epitaxy via chemical vapor deposition. *Nano Lett* 2011, 11:1106–1110.

25. Zhang Y, Tang T-T, Girit C, Hao Z, Martin MC, Zettl A, Crommie MF, Shen YR, Wang F. Direct observation of a widely tunable bandgap in bilayer graphene. *Nature* 2009, 459:820–823.

26. Guo Y, Guo W, Chen C. Tuning field-induced energy gap of bilayer graphene via interlayer spacing. *Appl Phys Lett* 2008, 92:243101.

27. Varchon F, Feng R, Hass J, Li X, Nguyen BN, Naud C, Mallet P, Veuillen JY, Berger C, Conrad EH. Electronic structure of epitaxial graphene layers on SiC: effect of the substrate. *Phys Rev Lett* 2007, 99:126805.

28. Mattausch A, Pankratov O. Ab initio study of graphene on SiC. *Phys Rev Lett* 2007, 99:076802.

29. Guo Y, Guo W, Chen C. Bias voltage induced n-to p-type transition in epitaxial bilayer graphene on SiC. *Phys Rev B* 2009, 80:085424.

30. Magda GZ, Jin X, Hagymási I, Vancsó P, Osváth Z, Nemes-Incze P, Hwang C, Biró LP, Tapasztó L. Room-temperature magnetic order on zigzag edges of narrow graphene nanoribbons. *Nature* 2014, 514:608–611.

31. Suenaga K, Koshino M. Atom-by-atom spectroscopy at graphene edge. *Nature* 2010, 468:1088–1090.

32. Wu W, Zhang Z, Lu P, Guo W. Electronic and magnetic properties of zigzag graphene nanoribbons with

periodic protruded edges. *Phys Rev B* 2010, 82:085425.

33. Yoon Y, Guo J. Effect of edge roughness in graphene nanoribbon transistors. *Appl Phys Lett* 2007, 91:073103.

34. Son Y-W, Cohen ML, Louie SG. Half-metallic graphene nanoribbons. *Nature* 2006, 444:347–349.

35. Yu J, Guo W. A new paradigm to half-metallicity in graphene nanoribbons. *J Phys Chem Lett* 2013, 4:951–955.

36. Zhang Z, Chen C, Guo W. Magnetoelectric effect in graphene nanoribbons on substrates via electric bias control of exchange splitting. *Phys Rev Lett* 2009, 103:187204.

37. E-j K, Li Z, Yang J, Hou JG. Half-metallicity in edge-modified zigzag graphene nanoribbons. *J Am Chem Soc* 2008, 130:4224–4225.

38. Dutta S, Manna AK, Pati SK. Intrinsic half-metallicity in modified graphene nanoribbons. *Phys Rev Lett* 2009, 102:096601.

39. Guo Y, Guo W, Chen C. Semiconducting to half-metallic to metallic transition on spin-resolved zigzag bilayer graphene nanoribbons. *J Phys Chem C* 2010, 114:13098–13105.

40. Zhang Z, Guo W. Electronic properties of zigzag graphene nanoribbons on Si (001). *Appl Phys Lett* 2009, 95:023107.

41. Sun L, Li Q, Ren H, Su H, Shi QW, Yang J. Strain effect on electronic structures of graphene nanoribbons: a first-principles study. *J Chem Phys* 2008, 129:074704.

42. Li Y, Jiang X, Liu Z, Liu Z. Strain effects in graphene and graphene nanoribbons: the underlying mechanism. *Nano Res* 2010, 3:545–556.

43. Gunlycke D, Li J, Mintmire JW, White CT. Edges bring new dimension to graphene nanoribbons. *Nano Lett* 2010, 10:3638–3642.

44. Zhang DB, Dumitrică T. Effective tensional strain driven bandgap modulations in helical graphene nanoribbons. *Small* 2011, 7:1023–1027.

45. Iijima S. Helical microtubules of graphitic carbon. *Nature* 1991, 354:56–58.

46. Sanchez-Valencia JR, Dienel T, Gröning O, Shorubalko I, Mueller A, Jansen M, Amsharov K, Ruffieux P, Fasel R. Controlled synthesis of single-chirality carbon nanotubes. *Nature* 2014, 512:61–64.

47. Yang F, Wang X, Zhang D, Yang J, Luo D, Xu Z, Wei J, Wang J-Q, Xu Z, Peng F. Chirality-specific growth of single-walled carbon nanotubes on solid alloy catalysts. *Nature* 2014, 510:522–524.

48. Minot ED, Yaish Y, Sazonova V, McEuen PL. Determination of electron orbital magnetic moments in carbon nanotubes. *Nature* 2004, 428:536–539.

49. Sun LF, Xie SS, Liu W, Zhou WY, Liu ZQ, Tang DS, Wang G, Qian LX. Materials: creating the narrowest carbon nanotubes. *Nature* 2000, 403:384.

50. Wang N, Tang Z-K, Li G-D, Chen JS. Materials science: Single-walled 4 Å carbon nanotube arrays. *Nature* 2000, 408:50–51.

51. Peng LM, Zhang ZL, Xue ZQ, Wu QD, Gu ZN, Pettifor DG. Stability of carbon nanotubes: how small can they be? *Phys Rev Lett* 2000, 85:3249.

52. Zhao X, Liu Y, Inoue S, Suzuki T, Jones RO, Ando Y. Smallest carbon nanotube is 3 Å in diameter. *Phys Rev Lett* 2004, 92:125502.

53. Pan ZW, Xie SS, Chang BH, Wang CY, Lu L, Liu W, Zhou WY, Li WZ, Qian LX. Very long carbon nanotubes. *Nature* 1998, 394:631–632.

54. Zhang R, Zhang Y, Zhang Q, Xie H, Qian W, Wei F. Growth of half-meter long carbon nanotubes based on Schulz-Flory distribution. *ACS Nano* 2013, 7:6156–6161.

55. Ruland W, Schaper AK, Hou H, Greiner A. Multi-wall carbon nanotubes with uniform chirality: evidence for scroll structures. *Carbon* 2003, 41:423–427.

56. Xu Z, Bai X, Wang ZL, Wang E. Multiwall carbon nanotubes made of monochirality graphite shells. *J Am Chem Soc* 2006, 128:1052–1053.

57. Koziol K, Shaffer M, Windle A. Three-dimensional internal order in multiwalled carbon nanotubes grown by chemical vapor deposition. *Adv Mater* 2005, 17:760–763.

58. Guo W, Guo Y. Energy optimum chiralities of multi-walled carbon nanotubes. *J Am Chem Soc* 2007, 129:2730–2731.

59. Blase X, Benedict LX, Shirley EL, Louie SG. Hybridization effects and metallicity in small radius carbon nanotubes. *Phys Rev Lett* 1994, 72:1878.

60. Treacy MJ, Ebbesen TW, Gibson JM. Exceptionally high Young's modulus observed for individual carbon nanotubes. *Nature* 1996, 381:678–680.

61. Yakobson BI, Brabec CJ, Bernholc J. Nanomechanics of carbon tubes: instabilities beyond linear response. *Phys Rev Lett* 1996, 76:2511.

62. Yu M-F, Lourie O, Dyer MJ, Moloni K, Kelly TF, Ruoff RS. Strength and breaking mechanism of multi-walled carbon nanotubes under tensile load. *Science* 2000, 287:637–640.

63. Lourie O, Cox DM, Wagner HD. Buckling and collapse of embedded carbon nanotubes. *Phys Rev Lett* 1998, 81:1638.

64. Shen W, Jiang B, Han BS, Xie S-s. Investigation of the radial compression of carbon nanotubes with a scanning probe microscope. *Phys Rev Lett* 2000, 84:3634.

65. Choi HJ, Ihm J, Louie SG, Cohen ML. Defects, quasi-bound states, and quantum conductance in metallic carbon nanotubes. *Phys Rev Lett* 2000, 84:2917.

66. Sammalkorpi M, Krasheninnikov A, Kuronen A, Nordlund K, Kaski K. Mechanical properties of carbon nanotubes with vacancies and related defects. *Phys Rev B* 2004, 70:245416.

67. Yang L, Han J. Electronic structure of deformed carbon nanotubes. *Phys Rev Lett* 2000, 85:154.

68. Minot ED, Yaish Y, Sazonova V, Park J-Y, Brink M, McEuen PL. Tuning carbon nanotube band gaps with strain. *Phys Rev Lett* 2003, 90:156401.

69. Guo W, Guo Y. Giant axial electrostrictive deformation in carbon nanotubes. *Phys Rev Lett* 2003, 91:115501.

70. Sazonova V, Yaish Y, Üstünel H, Roundy D, Arias TA, McEuen PL. A tunable carbon nanotube electromechanical oscillator. *Nature* 2004, 431:284–287.

71. Park C-J, Kim Y-H, Chang KJ. Band-gap modification by radial deformation in carbon nanotubes. *Phys Rev B* 1999, 60:10656.

72. Lu J-Q, Wu J, Duan W, Liu F, Zhu B-F, Gu B-L. Metal-to-semiconductor transition in squashed armchair carbon nanotubes. *Phys Rev Lett* 2003, 90:156601.

73. Mehrez H, Svizhenko A, Anantram MP, Elstner M, Frauenheim T. Analysis of band-gap formation in squashed armchair carbon nanotubes. *Phs Rev B* 2005, 71:155421.

74. Rochefort A, Avouris P, Lesage F, Salahub DR. Electrical and mechanical properties of distorted carbon nanotubes. *Phys Rev B* 1999, 60:13824.

75. Rochefort A, Salahub DR, Avouris P. The effect of structural distortions on the electronic structure of carbon nanotubes. *Chem Phys Lett* 1998, 297:45–50.

76. Kane CL, Mele EJ. Size, shape, and low energy electronic structure of carbon nanotubes. *Phys Rev Lett* 1997, 78:1932.

77. Chibotaru LF, Bovin SA, Ceulemans A. Bend-induced insulating gap in carbon nanotubes. *Phys Rev B* 2002, 66:161401.

78. Farajian AA, Yakobson BI, Mizuseki H, Kawazoe Y. Electronic transport through bent carbon nanotubes: nanoelectromechanical sensors and switches. *Phys Rev B* 2003, 67:205423.

79. Lee YHL, Kim SG, Tománek D. Field-induced unraveling of carbon nanotubes. *Chem Phys Lett* 1997, 265:667–672.

80. Li C, Chou T-W. Theoretical studies on the charge-induced failure of single-walled carbon nanotubes. *Carbon* 2007, 45:922–930.

81. Guo Y, Guo W. Mechanical and electrostatic properties of carbon nanotubes under tensile loading and electric field. *J Phys D Appl Phys* 2003, 36:805.

82. De Pablo PJ, Howell S, Crittenden S, Walsh B, Graugnard E, Reifenberger R. Correlating the location of structural defects with the electrical failure of multiwalled carbon nanotubes. *Appl Phys Lett* 1999, 75:3941.

83. Rueckes T, Kim K, Joselevich E, Tseng GY, Cheung C-L, Lieber CM. Carbon nanotube-based nonvolatile random access memory for molecular computing. *Science* 2000, 289:94–97.

84. Sun G, Kürti J, Kertesz M, Baughman RH. Dimensional changes as a function of charge injection in single-walled carbon nanotubes. *J Am Chem Soc* 2002, 124:15076–15080.

85. Baughman RH, Cui C, Zakhidov AA, Iqbal Z, Barisci JN, Spinks GM, Wallace GG, Mazzoldi A, De Rossi D, Rinzler AG. Carbon nanotube actuators. *Science* 1999, 284:1340–1344.

86. Ajiki H, Ando T. Electronic states of carbon nanotubes. *J Phys Soc Jpn* 1993, 62:1255–1266.

87. Song SN, Wang XK, Chang RPH, Ketterson JB. Electronic properties of graphite nanotubules from galvanomagnetic effects. *Phys Rev Lett* 1994, 72:697.

88. Ajiki H, Ando T. Magnetic properties of carbon nanotubes. *J Phys Soc Jpn* 1993, 62:2470–2480.

89. Zaric S, Ostojic GN, Kono J, Shaver J, Moore VC, Strano MS, Hauge RH, Smalley RE, Wei X. Optical signatures of the Aharonov-Bohm phase in single-walled carbon nanotubes. *Science* 2004, 304:1129–1131.

90. Zhang Z, Guo W. Magnetic properties of strained single-walled carbon nanotubes. *Appl Phys Lett* 2007, 90:053114.

91. Bachtold A, Strunk C, Salvetat J-P, Bonard J-M, Forró L, Nussbaumer T, Schönenberger C. Aharonov-Bohm oscillations in carbon nanotubes. *Nature* 1999, 397:673–675.

92. Coskun UC, Wei T-C, Vishveshwara S, Goldbart PM, Bezryadin A. h/e magnetic flux modulation of the energy gap in nanotube quantum dots. *Science* 2004, 304:1132–1134.

93. Cao J, Wang Q, Rolandi M, Dai H. Aharonov-Bohm interference and beating in single-walled carbon-nanotube interferometers. *Phys Rev Lett* 2004, 93:216803.

94. Zhang Y, Yu G, Dong J. Aharonov-Bohm interference and beating in deformed single-walled carbon nanotube interferometers. *Phys Rev B* 2006, 73:205419.

95. Cai JZ, Lu L, Kong WJ, Zhu HW, Zhang C, Wei BQ, Wu DH, Liu F. Pressure-induced transition in magnetoresistance of single-walled carbon nanotubes. *Phys Rev Lett* 2006, 97:026402.

96. Nosho Y, Ohno Y, Kishimoto S, Mizutani T. n-type carbon nanotube field-effect transistors fabricated by

using Ca contact electrodes. *Appl Phys Lett* 2005, 86:073105.

97. Ding L, Wang S, Zhang Z, Zeng Q, Wang Z, Pei T, Yang L, Liang X, Shen J, Chen Q. Y-contacted high-performance n-type single-walled carbon nanotube field-effect transistors: scaling and comparison with Sc-contacted devices. *Nano Lett* 2009, 9:4209–4214.

98. Tans SJ, Verschueren ARM, Dekker C. Room-temperature transistor based on a single carbon nanotube. *Nature* 1998, 393:49–52.

99. Martel R, Schmidt T, Shea HR, Hertel T, Avouris P. Single-and multi-wall carbon nanotube field-effect transistors. *Appl Phys Lett* 1998, 73:2447–2449.

100. Collins PG, Bradley K, Ishigami M, Zettl A. Extreme oxygen sensitivity of electronic properties of carbon nanotubes. *Science* 2000, 287:1801–1804.

101. Nardelli MB, Fattebert JL, Bernholc J. O (N) real-space method for ab initio quantum transport calculations: application to carbon nanotube-metal contacts. *Phys Rev B* 2001, 64:245423.

102. Okada S, Oshiyama A. Electronic structure of semiconducting nanotubes adsorbed on metal surfaces. *Phys Rev Lett* 2005, 95:206804.

103. Shan B, Cho K. Ab initio study of Schottky barriers at metal-nanotube contacts. *Phys Rev B* 2004, 70:233405.

104. Tans SJ, Devoret MH, Dai H, Thess A, Smalley RE, Georliga L, Dekker C. Individual single-wall carbon nanotubes as quantum wires. *Nature* 1997, 386:474–477.

105. Anantram MP, Datta S, Xue Y. Coupling of carbon nanotubes to metallic contacts. *Phys Rev B* 2000, 61:14219.

106. Lu Q, Rao R, Sadanadan B, Que W, Rao AM, Ke PC. Coupling of photon energy via a multiwalled carbon nanotube array. *Appl Phys Lett* 2005, 87:173102.

107. Nemec N, Tománek D, Cuniberti G. Contact dependence of carrier injection in carbon nanotubes: an ab initio study. *Phys Rev Lett* 2006, 96:076802.

108. Avouris P, Hertel T, Martel R, Schmidt T, Shea HR, Walkup RE. Carbon nanotubes: nanomechanics, manipulation, and electronic devices. *Appl Surf Sci* 1999, 141:201–209.

109. Orellana W, Miwa RH, Fazzio A. First-principles calculations of carbon nanotubes adsorbed on Si (001). *Phys Rev Lett* 2003, 91:166802.

110. Berber S, Oshiyama A. Atomic and electronic structures of carbon nanotubes on Si (001) stepped surfaces. *Phys Rev Lett* 2006, 96:105505.

111. Peng GW, Huan ACH, Liu L, Feng YP. Structural and electronic properties of 4 Å carbon nanotubes on Si (001) surfaces. *Phys Rev B* 2006, 74:235416.

112. Kim Y-H, Heben MJ, Zhang SB. Nanotube wires on commensurate InAs surfaces: binding energies, band alignments, and bipolar doping by the surfaces. *Phys Rev Lett* 2004, 92:176102.

113. Dean CR, Young AF, Meric I, Lee C, Wang L, Sorgenfrei S, Watanabe K, Taniguchi T, Kim P, Shepard KL. Boron nitride substrates for high-quality graphene electronics. *Nat Nanotechnol* 2010, 5:722–726.

114. Lu G, Wu T, Yuan Q, Wang H, Wang H, Ding F, Xie X, Jiang M. Synthesis of large single-crystal hexagonal boron nitride grains on Cu–Ni alloy. *Nat Commun* 2015, 6:6160.

115. Yin J, Liu X, Lu W, Li J, Cao Y, Li Y, Xu Y, Li X, Zhou J, Jin C, et al. Aligned growth of hexagonal boron nitride monolayer on germanium. *Small* 2015, 11:5375–5380.

116. Yin J, Yu J, Li X, Li J, Zhou J, Zhang Z, Guo W. Large single-crystal hexagonal boron nitride monolayer domains with controlled morphology and straight merging boundaries. *Small* 2015, 11:4497–4502.

117. Chopra NG, Luyken RJ, Cherrey K, Crespi VH, Cohen ML, Louie SG, Zettl A. Boron nitride nanotubes. *Science* 1995, 269:966–967.

118. Golberg D, Bando Y, Tang CC, Zhi CY. Boron nitride nanotubes. *Adv Mater* 2007, 19:2413–2432.

119. Hernandez E, Goze C, Bernier P, Rubio A. Elastic properties of C and $B_xC_yN_z$ composite nanotubes. *Phys Rev Lett* 1998, 80:4502.

120. Bettinger HF, Dumitrică T, Scuseria GE, Yakobson BI. Mechanically induced defects and strength of BN nanotubes. *Phys Rev B* 2002, 65:041406.

121. Dumitrică T, Yakobson BI. Rate theory of yield in boron nitride nanotubes. *Phys Rev B* 2005, 72:035418.

122. Terauchi M, Tanaka M, Suzuki K, Ogino A, Kimura K. Production of zigzag-type BN nanotubes and BN cones by thermal annealing. *Chem Phys Lett* 2000, 324:359–364.

123. Zhang Z, Guo W, Dai Y. Stability and electronic properties of small boron nitride nanotubes. *J Appl Phys* 2009, 105:084312.

124. Dai Y, Guo W, Zhang Z, Zhou B, Tang C. Electric-field-induced deformation in boron nitride nanotubes. *J Phys D Appl Phys* 2009, 42:085403.

125. Kim Y-H, Chang KJ, Louie SG. Electronic structure of radially deformed BN and BC_3 nanotubes. *Phys Rev B* 2001, 63:205408.

126. Khoo KH, Louie SG. Tuning the electronic properties of boron nitride nanotubes with transverse electric fields: a giant dc Stark effect. *Phys Rev B* 2004, 69:201401.

127. Chen C-W, Lee M-H, Clark SJ. Band gap modification of single-walled carbon nanotube and boron

nitride nanotube under a transverse electric field. *Nanotechnology* 2004, 15:1837.

128. Ishigami M, Sau JD, Aloni S, Cohen ML, Zettl A. Observation of the giant Stark effect in boron-nitride nanotubes. *Phys Rev Lett* 2005, 94:056804.

129. Tang C, Bando Y, Huang Y, Yue S, Gu C, Xu F, Golberg D. Fluorination and electrical conductivity of BN nanotubes. *J Am Chem Soc* 2005, 127:6552–6553.

130. Zhi C, Bando Y, Tang C, Golberg D. Engineering of electronic structure of boron-nitride nanotubes by covalent functionalization. *Phys Rev B* 2006, 74:153413.

131. Zhang Z, Guo W. Tunable ferromagnetic spin ordering in boron nitride nanotubes with topological fluorine adsorption. *J Am Chem Soc* 2009, 131:6874–6879.

132. Golberg D, Bando Y, Kurashima K, Sato T. Ropes of BN multi-walled nanotubes. *Solid State Commun* 2000, 116:1–6.

133. Okada S, Saito S, Oshiyama A. Interwall interaction and electronic structure of double-walled BN nanotubes. *Phys Rev B* 2002, 65:165410.

134. Zhang Z-H, Guo W-L, Yakobson BI. Electromechanical coupling effect on electronic properties of double-walled boron nitride nanotubes. *Acta Mech Sin* 2012, 28:1532–1538.

135. Zhang Z, Zeng XC, Guo W. Homogeneous nanocables from double-walled boron-nitride nanotubes using first-principles calculations. *Phys Rev B* 2010, 82:035412.

136. Zhang Z, Guo W, Yakobson BI. Self-modulated band gap in boron nitride nanoribbons and hydrogenated sheets. *Nanoscale* 2013, 5:6381–6387.

137. Zeng H, Zhi C, Zhang Z, Wei X, Wang X, Guo W, Bando Y, Golberg D. "White graphenes": boron nitride nanoribbons via boron nitride nanotube unwrapping. *Nano Lett* 2010, 10:5049–5055.

138. Chatterjee S, Luo Z, Acerce M, Yates DM, Johnson AC, Sneddon LG. Chemical vapor deposition of boron nitride nanosheets on metallic substrates via decaborane/ammonia reactions. *Chem Mater* 2011, 23:4414–4416.

139. Park C-H, Louie SG. Energy gaps and stark effect in boron nitride nanoribbons. *Nano Lett* 2008, 8:2200–2203.

140. Barone V, Peralta JE. Magnetic boron nitride nanoribbons with tunable electronic properties. *Nano Lett* 2008, 8:2210–2214.

141. Chen W, Li Y, Yu G, Li C-Z, Zhang SB, Zhou Z, Chen Z. Hydrogenation: a simple approach to realize semiconductor-half-metal-metal transition in boron nitride nanoribbons. *J Am Chem Soc* 2010, 132:1699–1705.

142. Li X, Wu X, Zeng XC, Yang J. Band-gap engineering via tailored line defects in boron-nitride nanoribbons, sheets, and nanotubes. *ACS Nano* 2012, 6:4104–4112.

143. Tang S, Zhang S. Electronic and magnetic properties of hybrid boron nitride nanoribbons and sheets with 5–7 Line defects. *J Phys Chem C* 2013, 117:17309–17318.

144. Lopez-Bezanilla A, Huang J, Terrones H, Sumpter BG. Boron nitride nanoribbons become metallic. *Nano Lett* 2011, 11:3267–3273.

145. Qi J, Qian X, Qi L, Feng J, Shi D, Li J. Strain-engineering of band gaps in piezoelectric boron nitride nanoribbons. *Nano Lett* 2012, 12:1224–1228.

146. Feng C, Mi Z, Zhong J-X. Strain effect on transport properties of hexagonal boron–nitride nanoribbons. *Chin Phys B* 2010, 19:086105.

147. Zhang Z, Guo W. Intrinsic metallic and semiconducting cubic boron nitride nanofilms. *Nano Lett* 2012, 12:3650–3655.

148. Zhang Z, Zeng XC, Guo W. Fluorinating hexagonal boron nitride into diamond-like nanofilms with tunable band gap and ferromagnetism. *J Am Chem Soc* 2011, 133:14831–14838.

149. Guo Y, Guo W. Insulating to metallic transition of an oxidized boron nitride nanosheet coating by tuning surface oxygen adsorption. *Nanoscale* 2014, 6:3731–3736.

150. Guo Y, Guo W. Magnetism in oxygen-functionalized hexagonal boron nitride nanosheet on copper substrate. *J Phys Chem C* 2015, 119:873–878.

151. Ganatra R, Zhang Q. Few-layer MoS_2: a promising layered semiconductor. *ACS Nano* 2014, 8:4074–4099.

152. Chhowalla M, Shin HS, Eda G, Li L-J, Loh KP, Zhang H. The chemistry of two-dimensional layered transition metal dichalcogenide nanosheets. *Nat Chem* 2013, 5:263–275.

153. Conley HJ, Wang B, Ziegler JI, Haglund RF Jr, Pantelides ST, Bolotin KI. Bandgap engineering of strained monolayer and bilayer MoS_2. *Nano Lett* 2013, 13:3626–3630.

154. Hui YY, Liu X, Jie W, Chan NY, Hao J, Hsu Y-T, Li L-J, Guo W, Lau SP. Exceptional tunability of band energy in a compressively strained trilayer MoS_2 sheet. *ACS Nano* 2013, 7:7126–7131.

155. Shi H, Pan H, Zhang Y-W, Yakobson BI. Quasiparticle band structures and optical properties of strained monolayer MoS_2 and WS_2. *Phys Rev B* 2013, 87:155304.

156. Mattheiss L. Band structures of transition-metal-dichalcogenide layer compounds. *Phys Rev B* 1973, 8:3719.

157. Mak KF, Lee C, Hone J, Shan J, Heinz TF. Atomically thin MoS_2: a new direct-gap semiconductor. *Phys Rev Lett* 2010, 105:136805.

158. Han S, Kwon H, Kim SK, Ryu S, Yun WS, Kim D, Hwang J, Kang J-S, Baik J, Shin H. Band-gap transition induced by interlayer van der Waals interaction in MoS_2. *Phys Rev B* 2011, 84:045409.

159. Lu P, Wu X, Guo W, Zeng XC. Strain-dependent electronic and magnetic properties of MoS_2 monolayer, bilayer, nanoribbons and nanotubes. *Phys Chem Chem Phys* 2012, 14:13035–13040.

160. Scalise E, Houssa M, Pourtois G, Afanas'ev V, Stesmans A. Strain-induced semiconductor to metal transition in the two-dimensional honeycomb structure of MoS_2. *Nano Res* 2012, 5:43–48.

161. Johari P, Shenoy VB. Tuning the electronic properties of semiconducting transition metal dichalcogenides by applying mechanical strains. *ACS Nano* 2012, 6:5449–5456.

162. Dou X, Ding K, Jiang D, Sun B. Tuning and identification of interband transitions in monolayer and bilayer molybdenum disulfide using hydrostatic pressure. *ACS Nano* 2014, 8:7458–7464.

163. Alvarez MP, del Corro E, Morales García Á, Kavan L, Kalbac M, Frank O. Single layer molybdenum disulfide under direct out-of-plane compression: Low-stress band-gap engineering. *Nano Lett* 2015, 15:3139–3146.

164. Nayak AP, Bhattacharyya S, Zhu J, Liu J, Wu X, Pandey T, Jin C, Singh AK, Akinwande D, Lin J-F. Pressure-induced semiconducting to metallic transition in multilayered molybdenum disulphide. *Nat Commun* 2014, 5:3731.

165. Chi Z-H, Zhao X-M, Zhang H, Goncharov AF, Lobanov SS, Kagayama T, Sakata M, Chen X-J. Pressure-induced metallization of molybdenum disulfide. *Phys Rev Lett* 2014, 113:036802.

166. Tongay S, Zhou J, Ataca C, Lo K, Matthews TS, Li J, Grossman JC, Wu J. Thermally driven crossover from indirect toward direct bandgap in 2D semiconductors: $MoSe_2$ versus MoS_2. *Nano Lett* 2012, 12:5576–5580.

167. Ataca C, Sahin H, Ciraci S. Stable, single-layer MX_2 transition-metal oxides and dichalcogenides in a honeycomb-like structure. *J Phys Chem C* 2012, 116:8983–8999.

168. Ma Y, Dai Y, Guo M, Niu C, Zhu Y, Huang B. Evidence of the existence of magnetism in pristine VX_2 monolayers (X=S, Se) and their strain-induced tunable magnetic properties. *ACS Nano* 2012, 6:1695–1701.

169. Xu Y, Liu X, Guo W. Tensile strain induced switching of magnetic states in $NbSe_2$ and NbS_2 single layers. *Nanoscale* 2014, 6:12929–12933.

170. Manchanda P, Sharma V, Yu H, Sellmyer D, Skomski R. Magnetism of Ta dichalcogenide monolayers tuned by strain and hydrogenation. *Appl Phys Lett* 2015, 107:032402.

171. Huang Y, Ling C, Liu H, Wang S, Geng B. Versatile electronic and magnetic properties of $SnSe_2$ nanostructures induced by the strain. *J Phys Chem C* 2014, 118:9251–9260.

172. Wang Z, Zhao K, Li H, Liu Z, Shi Z, Lu J, Suenaga K, Joung S-K, Okazaki T, Jin Z. Ultranarrow WS_2 nanoribbons encapsulated in carbon nanotubes. *J Mater Chem* 2011, 21:171–180.

173. Gao D, Xue Q, Mao X, Wang W, Xu Q, Xue D. Ferromagnetism in ultrathin VS_2 nanosheets. *J Mater Chem C* 2013, 1:5909–5916.

174. Novoselov K, Jiang D, Schedin F, Booth T, Khotkevich V, Morozov S, Geim A. Two-dimensional atomic crystals. *Proc Natl Acad Sci USA* 2005, 102:10451–10453.

175. Coleman JN, Lotya M, O'Neill A, Bergin SD, King PJ, Khan U, Young K, Gaucher A, De S, Smith RJ. Two-dimensional nanosheets produced by liquid exfoliation of layered materials. *Science* 2011, 331:568–571.

176. Li L, Yu Y, Ye GJ, Ge Q, Ou X, Wu H, Feng D, Chen XH, Zhang Y. Black phosphorus field-effect transistors. *Nat Nanotechnol* 2014, 9:372–377.

177. Liu H, Neal AT, Zhu Z, Luo Z, Xu X, Tománek D, Ye PD. Phosphorene: an unexplored 2D semiconductor with a high hole mobility. *ACS Nano* 2014, 8:4033–4041.

178. Fei R, Yang L. Strain-engineering the anisotropic electrical conductance of few-layer black phosphorus. *Nano Lett* 2014, 14:2884–2889.

179. Li Y, Yang S, Li J. Modulation of the electronic properties of ultrathin black phosphorus by strain and electrical field. *J Phys Chem C* 2014, 118:23970–23976.

180. Wei Q, Peng X. Superior mechanical flexibility of phosphorene and few-layer black phosphorus. *App Phys Lett* 2014, 104:251915.

181. Kou L, Chen C, Smith SC. Phosphorene: fabrication, properties, and applications. *J Phys Chem Lett* 2015, 6:2794–2805.

182. Ling X, Wang H, Huang S, Xia F, Dresselhaus MS. The renaissance of black phosphorus. *Proc Natl Acad Sci USA* 2015, 112:4523–4530.

183. Peng X, Wei Q, Copple A. Strain-engineered direct–indirect band gap transition and its mechanism in two-dimensional phosphorene. *Phys Rev B* 2014, 90:085402.

184. Lv H, Lu W, Shao D, Sun Y. Enhanced thermoelectric performance of phosphorene by strain-induced band convergence. *Phys Rev B* 2014, 90:085433.

185. Liu Q, Zhang X, Abdalla LB, Fazzio A, Zunger A. Switching a normal insulator into a topological insulator via electric field with application to phosphorene. *Nano Lett* 2015, 15:1222–1228.

186. Guo H, Lu N, Dai J, Wu X, Zeng XC. Phosphorene nanoribbons, phosphorus nanotubes, and van der Waals multilayers. *J Phys Chem C* 2014, 118:14051–14059.

187. Tran V, Yang L. Scaling laws for the band gap and optical response of phosphorene nanoribbons. *Phys Rev B* 2014, 89:245407.

188. Morgan Stewart H, Shevlin SA, Catlow CRA, Guo ZX. Compressive straining of bilayer phosphorene leads to extraordinary electron mobility at a new conduction band edge. *Nano Lett* 2015, 15:2006–2010.

189. Naguib M, Mochalin VN, Barsoum MW, Gogotsi Y. 25th anniversary article: MXenes: a new family of two-dimensional materials. *Adv Mater* 2014, 26:992–1005.

190. Zhang X, Ma Z, Zhao X, Tang Q, Zhou Z. Computational studies on structural and electronic properties of functionalized MXene monolayers and nanotubes. *J Mater Chem A* 2015, 3:4960–4966.

191. Weng H, Ranjbar A, Liang Y, Song Z, Khazaei M, Yunoki S, Arai M, Kawazoe Y, Fang Z, Dai X. Large-gap two-dimensional topological insulator in oxygen functionalized MXene. *Phys Rev B* 2015, 92:075436.

192. Ma Z, Hu Z, Zhao X, Tang Q, Wu D, Zhou Z, Zhang L. Tunable band structures of heterostructured bilayers with transition-metal dichalcogenide and MXene monolayer. *J Phys Chem C* 2014, 118:5593–5599.

193. Zhao S, Kang W, Xue J. Manipulation of electronic and magnetic properties of M_2C (M=Hf, Nb, Sc, Ta, Ti, V, Zr) monolayer by applying mechanical strains. *Appl Phys Lett* 2014, 104:133106.

194. Cahangirov S, Topsakal M, Aktürk E, Şahin H, Ciraci S. Two-and one-dimensional honeycomb structures of silicon and germanium. *Phys Rev Lett* 2009, 102:236804.

195. Ni Z, Liu Q, Tang K, Zheng J, Zhou J, Qin R, Gao Z, Yu D, Lu J. Tunable bandgap in silicene and germanene. *Nano Lett* 2011, 12:113–118.

196. Tao L, Cinquanta E, Chiappe D, Grazianetti C, Fanciulli M, Dubey M, Molle A, Akinwande D. Silicene field-effect transistors operating at room temperature. *Nat Nanotechnol* 2015, 10:227–231.

197. Zhang S, Yan Z, Li Y, Chen Z, Zeng H. Atomically thin arsenene and antimonene: semimetal–semiconductor and indirect–direct band-gap transitions. *Angew Chem Int Ed* 2015, 127:3155–3158.

198. Botello-Méndez AR, López-Urías F, Terrones M, Terrones H. Magnetic behavior in zinc oxide zigzag nanoribbons. *Nano Lett* 2008, 8:1562–1565.

199. Kou L, Li C, Zhang Z, Guo W. Tuning magnetism in zigzag ZnO nanoribbons by transverse electric fields. *ACS Nano* 2010, 4:2124–2128.

200. Kou L, Li C, Zhang Z, Guo W. Electric-field- and hydrogen-passivation-induced band modulations in armchair ZnO nanoribbons. *J Phys Chem C* 2009, 114:1326–1330.

201. Zhang Z, Liu X, Yakobson BI, Guo W. Two-dimensional tetragonal TiC monolayer sheet and nanoribbons. *J Am Chem Soc* 2012, 134:19326–19329.

202. Zeng H, Dai J, Yao W, Xiao D, Cui X. Valley polarization in MoS_2 monolayers by optical pumping. *Nat Nanotechnol* 2012, 7:490–493.

203. Mak KF, He K, Shan J, Heinz TF. Control of valley polarization in monolayer MoS_2 by optical helicity. *Nat Nanotechnol* 2012, 7:494–498.